RSC Advances

This article can be cited before page numbers have been issued, to do this please use: A. Girgis, S. S. Panda, M. N. Aziz, P. Steel, C. D. Hall and A. R. Katritzky, *RSC Adv.*, 2015, DOI: 10.1039/C4RA16663A.

ROYAL SOCIETY OF CHEMISTRY

www.rsc.org/advances

View Article Online
DOI: 10.1039/C4RA16663A

RSC Advances

RSCPublishing

PAPER

Rational design, synthesis, and 2D-QSAR study of anti-oncological alkaloids against hepatoma and cervical carcinoma

Cite this: DOI: 10.1039/xoxxoooooox

Adel S. Girgis,[a] Siva S. Panda,[b] Marian N. Aziz,[a] Peter J. Steel,[c] C. Dennis Hall*[,b] and Alan R. Katritzky[b,d]

Received ooth January 2012,
Accepted ooth January 2012

DOI: 10.1039/xoxxoooooox

www.rsc.org/

Antitumor active dispiro[3*H*-indole-3,2'-pyrrolidine-3',3''-piperidine]-2(1*H*),4''-diones **11-19** were regioselectively synthesized *via* azomethine ylide cycloaddition reactions with 3*E*,5*E*-1-alkyl-3,5-bis(arylmethylidene)-4-piperidones **3-7**. Compounds **13**, **14**, and **16** reveal higher potency against HeLa (cervical) tumor cell line than the standard reference cisplatin while, **11**, and **12** seem more potent against HepG2 (liver) carcinoma cell line relative to the standard reference doxorubicin hydrochloride as determined by *in-vitro* Sulfo-Rhodamine-B bio-assay. 3D-Pharmacophores of the HeLa comprise five chemical features *viz.* two hydrogen bond acceptors, two hydrophobic centers and one positive ionizable center and HepG2 contains three chemical features *viz.* a hydrogen bond acceptor, a hydrophobic center and a positive ionizable center. These features of the tumor cell lines explain the variation of bioactivity relative to chemical structure. Statistically significant QSAR models describing the spiro-alkaloid bio-properties were obtained employing CODESSA-Pro software validating the observed pharmacological observations and identifying the most important parameters governing activity.

Introduction

Although there has been progress in diagnosing, treating and managing cancer, the disease still results in the death of a significant number of patients. It remains the second leading cause of death worldwide after cardiovascular disease. The worldwide cancer burden is expected to increase by as much as 15 million new cases per year by 2020, according to the World Health Organization, unless further preventive measures are put into practice.[1,2] Generally, cancers of the breast, lung, colorectal, and prostate are the most frequent types in developed countries and cancers of the stomach, liver, oral cavity, and cervix the most frequent in developing countries, although these patterns are changing, especially due to population aging and life style changes.[3,4]. The preliminary cancer treatment options usually remain a combination of radiotherapy, surgery and chemotherapy. Chemotherapy is considered one of the effective approaches in suppressing tumor growth and eradication of tumors. However, many patients undergoing chemotherapy suffer from side effects such as nausea, vomiting, cachexia, lethargy and poor oral intake.[5] In spite of availability of a large number of anticancer drugs, the development of new chemotherapeutics is one of the most noteworthy challenges due to non-selectivity and emergence of resistance by cancerous cells towards existing anticancer agents. Therefore, a constant need to develop better alternatives to such problems is in demand.[6]

Recently we described regioselective synthesis of fluoro-substituted dispiro-oxindole and the structure was investigated by X-ray and theoretical studies.[7] We now report full details of the synthesis of spiro-indoles within the present work were bio-assayed for their anti-oncological properties against human cervical (HeLa), and hepatoma (HepG2) cancer cell lines, and the rationale for this is as follows. Cervical carcinoma is the third most common cancer and the fourth leading cause of cancer-related death in women worldwide; every year, approximately 529,800 new cases are diagnosed, and approximately 275,000 women die from this disease.[8,9] More than 80% of cervical cancer cases occur in developing countries, while incidence and mortality have substantially declined in developed countries.[10,11] Persistent infections with oncogenic types of human papillomavirus (HPV) are the main risk factors for cervical cancer development.[12] From almost 160 HPV types that have been characterized,[13] close to 30 infect the anogenital epithelium and 14 of them have been classified as oncogenic types.[14,15] The biological behavior of HPV infections is influenced by viral cellular and host factors and

Paper View Article Online DOI: 10.1039/C4RA16663A RSC Advances

varies in different lesions, even when the same viral type is involved.[16] Human cervical cancer cells can be categorized according to HPV type as HeLa (HPV-18+), ME-180 (HPV-68+), SiHa (HPV-16+), and SW756 (HPV-18+) cells.[17–19] Although several advances in screening, diagnostic and treatment modalities have been made, the overall prognosis of cervical cancer has not changed dramatically, and the mortality rate still approaches 50%. The treatment of choice of cervical cancer is represented by radiotherapy or surgery for early stage disease and concurrent chemoradiation for advanced stage patients.[20] Concurrent chemotherapy and radiotherapy (CCRT) is the standard of care for locally advanced cervical cancer, able to achieve a 6% improvement in a 5-year survival compared to radiotherapy alone.[21–23] A larger survival advantage occurs when adjuvant chemotherapy is administered after CCRT.[23–25] Cisplatin is the drug of choice either alone or in combination with topotecan.[26] The combination of cisplatin with 5-fluorouracil has also been reported.[27,28] However, severe side-effects like bone-marrow depression, neutropenia, thrombocytopenia and anaemia due to haematological toxicity along with nephrotoxicity and neurotoxicity[29] and acquired chemoresistance[30] throughout the course of treatment have limited the usage of cisplatin. Other reports describe the severe renal toxicity and gastrointestinal side effects of cisplatin that limits its application in clinic.[31]

Liver malignancies including hepatocellular carcinoma, cholangiocarcinoma and hepatoblastoma are jointly the fifth most prevalent form of cancer and globally the third leading cause of cancer related death, immediately after mortality due to lung cancer and colon cancer.[32] In addition, the liver is a favorite site for metastasis of other cancers, in particular colorectal cancer, esophageal cancer and pancreatic cancer. The five-year natural mortality rate for hepatocellular carcinoma is more than 95%, and it affects more than 500,000 people worldwide per year.[33] The major risk factors for liver cancer are persistent infection with hepatitis B virus (HBV) and hepatitis C virus (HCV), both of which increase the risk of liver cancer some 20-fold.[34] Other well-established liver cancer risk factors include cirrhosis, aflatoxin exposure, heavy alcohol drinking, tobacco smoking and some rare monogenic syndromes such as hereditary hemochromatosis and α-1 antitrypsin deficiency.[35] Doxorubicin (also named as adriamycin, ADR) has a broad antitumor effect as a typical DNA intercalating agent, and is often used as the first-line anticancer drug in treatment of acute leukemia, malignant lymphoma, multiple myeloma, breast cancer, osteosarcoma, soft tissue sarcoma and liver cancer.[36] The clinical application of doxorubicin is limited by its toxicity to normal tissues and cells, especially its cardiotoxicity.[37] The only clinically approved chemotherapy drug for advanced hepatocellular carcinoma is sorafenib, which shows only modest efficacy, improving survival of patients by just 3 months.[38,39]

3D-QSAR pharmacophoric generation and 2D-QSAR (quantitative structure-activity relationship) study is considered in the present work utilizing Discovery Studio 2.5 and Comprehensive Descriptors for Structural and Statistical Analysis (CODESSA-Pro) software. This allows a better understanding of the observed pharmacological activity and determines the most important structural parameters controlling bio-activity. These studies are also used to validate the observed bio-data.

Results and Discussion

Chemistry

3*E*,5*E*-1-Alkyl-3,5-bis(arylmethylidene)-4-piperidones **3-7**, the starting agents for constructing the targeted spiro-alkaloids, were synthesized *via* base-catalyzed condensation of 1-alkyl-4-piperidones **1,2** with aromatic aldehydes (Scheme 1). Due to the huge melting point difference (≈30 °C) between the literature reported[40] 3*E*,5*E*-3,5-bis[(2,4-dichlorophenyl)methylidene]-1-ethyl-4-piperidones **3** and our synthesized analogue, the structure of the compound was investigated using a variety of spectroscopic techniques. The IR spectrum of **3** reveals a strong stretching vibration band at ν = 1674 cm^{-1} assignable to the α,β-unstaurated ketonic function. The ^{1}H-NMR spectrum of **3** exhibits the exocyclic olefinic methine protons as a sharp singlet signal at δ = 7.91 confirming the formation of a single geometrical isomer (3*E*,5*E*).[41] The ^{13}C-NMR spectrum of **3** shows the olefinic methine carbon at δ = 136.1, and the carbonyl carbon at δ = 186.3. A single crystal X-ray study of **3** shows a half chair form conformation for the piperidinyl ring. The exocyclic olefinic bonds at *C*-3 and *C*-5 of the piperidinyl ring possess *E*,*E'*-configurations (Figure 1).

[3+2]-Cycloaddition of non-stabilized azomethine ylides (generated *in situ via* decarboxylative condensation of isatins **8-9** with sarcosine **10**) and 3*E*,5*E*-1-alkyl-3,5-bis(arylmethylidene)-4-piperidones **3-7** in refluxing ethanol proceeds regioselectively to afford single products (silica gel TLC) in good to excellent yields (62-98%) obeying the reported procedure.[42] The structure of the isolated products was assigned as 1''-alkyl-4'-aryl-5''-(arylmethylidene)-1'-methyl-dispiro[3*H*-indole-3,2'-pyrrolidine-3',3''-piperidine]-2(1*H*),4''-diones **11-19** based on their spectroscopic (IR, ^{1}H-, ^{13}C-NMR, ^{1}H, ^{1}H-COSY, HSQC, HRMS) data and elemental analysis (Figures S1-S32 of supplementary material). The reaction commences with nucleophilic attack of the amino group of sarcosine **10** on the 3-carbonyl function of isatin **8-9**, followed by dehydration to form a spiro-oxazalidinone system. This, expels carbon dioxide to generate a reactive, non-stabilized azomethine ylide, that undergoes *in situ* 1,3-dipolar cycloaddition to the exocyclic olefinic linkage of piperidones **3-7** affording eventually spiro-alkaloids **11-19** (Scheme 2).

RSC Advances
View Article Online
DOI: 10.1039/C4RA16633J
Paper

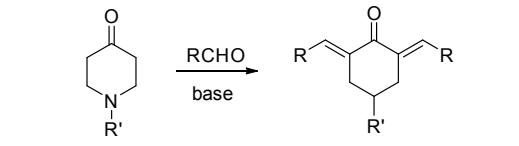

1-2 **3-7**

1 R' = Me
2 R' = Et

3 R = 2,4-$Cl_2C_6H_3$, R' = Et
4 R = 4-FC_6H_4, R' = Et
5 R = 2-thienyl, R' = Et
6 R = 3-pyridinyl, R' = Me
7 R = 3-pyridinyl, R' = Et

Scheme 1 Synthetic route towards 3*E*,5*E*-1-alkyl-3,5-bis(arylmethylidene)-4-piperidones **3-7**.

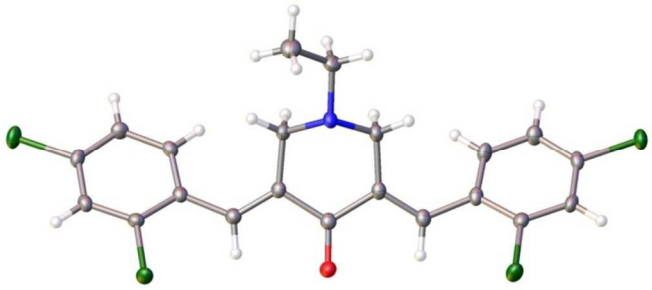

Figure 1 X-Ray crystal structure of compound **3**.

The IR spectrum of **11**, representative of the family, exhibits an indolyl amidic NH stretching vibration band at ν = 3285 cm^{-1}, and strong stretching vibration bands at ν = 1701 and 1678 cm^{-1} corresponding to the carbonyl of ketonic and amidic functions, respectively. The methylene protons H_2C-5', H_2C-2" and H_2C-6" of **11** are diastereotopic. The methylene protons of the ethyl group attached at the piperidinyl *N*-1" appear as a multiplet at δ = 1.93-2.11, due to mutual coupling with each other and in turn with the vicinal methyl protons (diastereotopic protons). The ^{13}C-NMR spectrum of **11** reveals the methylene carbons H_2C-6", H_2C-5' and H_2C-2" at δ = 53.4, 57.0, 56.1, respectively. The methine *HC*-4' is observed at δ = 41.3 and the spiro-carbons *C*-3' (*C*-3") and *C*-3 (*C*-2') are exhibited at δ = 62.1, 76.2, respectively. The carbonyl carbons *C*-2 and *C*-4" appear at δ = 176.3, 196.8, respectively. ^{1}H, ^{1}H-COSY spectrum (Figure S31 of supplementary material) and ^{1}H,^{13}C-heteronuclear single quantum coherence (HSQC) spectrum of compound **14** (Figures S32A, S32B of supplementary material) support these interpretations.

A single crystal X-ray study of **14** (Figure 2), supports the stereochemical structure. The indolyl as well as the 4-fluorophenyl rings have planar configurations and the exocyclic olefinic double bond has the *E*-configuration. The pyrrolidine ring has an envelope conformation with the flap atom being the ring nitrogen which is out of the plane of the remaining four atoms.

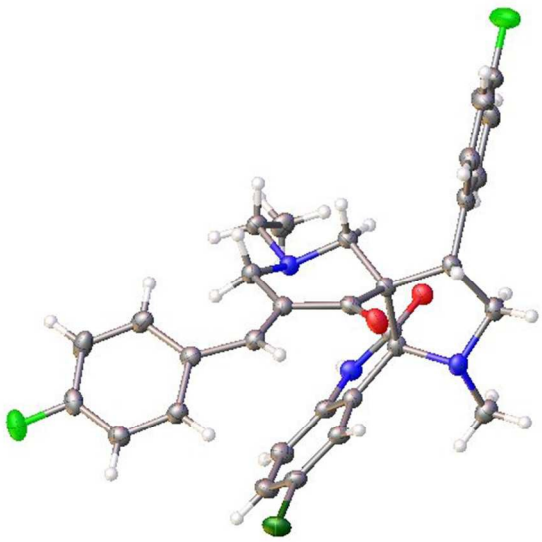

Figure 2 X-Ray crystal structure of compound **14**.

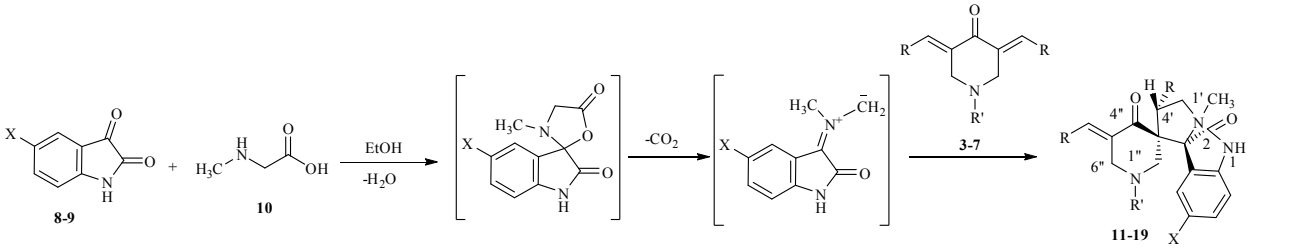

8-9

8 X = H
9 X = Cl

10

3 R = 2,4-$Cl_2C_6H_3$, R' = Et
4 R = 4-FC_6H_4, R' = Et
5 R = 2-thienyl, R' = Et
6 R = 3-pyridinyl, R' = Me
7 R = 3-pyridinyl, R' = Et

11-19

11 R = 2,4-$Cl_2C_6H_3$, R' = Et, X = H
12 R = 2,4-$Cl_2C_6H_3$, R' = Et, X = Cl
13 R = 4-FC_6H_4, R' = Et, X = H
14 R = 4-FC_6H_4, R' = Et, X = Cl
15 R = 2-thienyl, R' = Et, X = H
16 R = 2-thienyl, R' = Et, X = Cl
17 R = 3-pyridinyl, R' = Me, X = H
18 R = 3-pyridinyl, R' = Et, X = H
19 R = 3-pyridinyl, R' = Et, X = Cl

Scheme 2 Synthetic route towards dispiro[3*H*-indole-3,2'-pyrrolidine-3',3"-piperidines] **11-19**.

View Article Online
DOI: 10.1039/C4RA16663A RSC Advances

Antitumor properties

Antitumor properties of the synthesized dispiro[3*H*-indole-3,2'-pyrrolidine-3',3''-piperidines] **11-19** were screened against HeLa (cervical), and HepG2 (liver) human tumor cell lines utilizing the reported *in-vitro* Sulfo-Rhodamine-B standard method.[43–49] The results in Table 1 (Figures S33, and S34 of supplementary material) show that, all the synthesized compounds have considerable antitumor activity against the tested cell lines with variable potencies. Compounds **13, 14,** and **16** reveal higher potency (IC_{50} = 4.87, 5.75, and 7.25 μM, respectively) against HeLa (cervical) cell line than the standard reference cisplatin (IC_{50} = 7.71 μM) (clinically used against cervical carcinoma[26]). On the other hand, compounds **11**, and **12** seem more potent (IC_{50} = 3.53, and 7.20 μM, respectively) than doxorubicin hydrochloride (IC_{50} = 8.05μM) (clinically applicable agent against liver carcinoma[36]).

Structure-activity relationships (SAR) based on the observed antitumor activity data against HeLa (cervical carcinoma) reveal that the nature of the substituent attached to the phenyl group at *C*-4' and consequently the exocyclic olefinic linkage, seems to be a controlling factor governing the antitumor properties. Substitution of this phenyl group by fluorine atom enhances the observed antitumor properties more than two chlorine atoms, as exhibited in pairs **11**, **13** (IC_{50} = 16.69, 4.87 μM, respectively), and **12**, **14** (IC_{50} = 12.71, 5.75 μM, respectively).

SAR due to the observed antitumor activity data against HepG2 (liver carcinoma) cell line describes a contrast behavior than the aforementioned cervical cell line. 2,4-Dichlorophenyl substituent at *C*-4' and consequently the exocyclic olefinic linkage, seems the best choice for constructing antitumor active against hepatocellular carcinoma compared with the 4-fluorophenyl group as exhibited in pairs **11, 13** (IC_{50} = 3.53, 10.90 μM, respectively), and **12**, **14** (IC_{50} = 7.20, 12.50 μM, respectively). Additionally, the 3-pyridinyl group at *C*-4' and consequently the exocyclic olefinic linkage, seem to optimize antitumor activity against HepG2 (liver carcinoma) when compared with the thienyl group as exhibited in pairs **15, 18** (IC_{50} = 18.42, 17.04 μM, respectively), and **16**, **19** (IC_{50} = 17.34, 11.50 μM, respectively). This can be attributed to the π-deficient heterocyclic properties of the 3-pyridinyl group compared with the electron-donating properties of thienyl group.

In order to better understand the observed antitumor properties and determine the most important structural parameters controlling bio-activity, computational chemistry studies were undertaken. Additionally, validation of the observed antitumor properties was established *via* these studies.

Computational chemistry

3D-Pharmacophore modeling

The pharmacophore modeling technique has been widely used in lead discovery and optimization as a key tool in computer aided drug design. The 3D-pharmacophore study was performed using Discovery Studio 2.5 software (Accelrys Inc., San Diego, CA, USA) which permits 3D-pharmacophore generation, structural alignment, activity prediction and 3D-database creation.[45,50–52] A 3D-QSAR pharmacophore protocol was used to generate predictive pharmacophores *via* aligning different conformations in which the molecules are likely to bind with the receptor. A given hypothesis may be combined with known activity data to create a 3D-pharmacophore model that identifies overall aspects of molecular structure governing activity. 3D-QSAR pharmacophore was constructed using collections of molecules with activities ranging over a number of orders of magnitude. Pharmacophores explain the variability of bioactivity with respect to the geometric localization of the chemical features present in the molecules. The observed HYPOGEN identifies a 3D-array of five chemical features in the case of HeLa (cervical) and 3 features in case of HepG2 (liver) tumor cell lines which are common to the bio-active set compounds **11-19** that are consistent with binding to a proposed common receptor site.

The five chemical features of the HeLa pharmacophore are two hydrogen bond acceptors (HBA-1, HB-2), two hydrophobic centers (H-1, H-2), and one positive ionizable (PosIon) (Figure 3, Table 2 exhibits constraint distances and angles between features of the generated 3D-pharmacophore). On the other hand, the HepG2 pharmacophore contains three chemical features, a hydrogen bond acceptor (HBA), a hydrophobic (H) and a positive ionizable (PosIon) (Figure 4, Table 2). Table 3 exhibits fit values and estimated/predicted activities of the synthesized compounds **11-19** due to the generated 3D-pharmacophore models. Through the pharmacophore mapping study (Figures S35, S36 of supplementary material) it has been found that the major structural factors affecting the potency of the synthesized compounds are related to their basic skeleton. Additionally, most of the estimated activity as well as the fit values derived from the generated pharmacophores correlate with the experimentally observed potency. For example, the most potent analogue **13** (R = 4-FC_6H_4, R' = Et, X = H; IC_{50} = 4.87 μM) among all the synthesized compounds, shows an estimated potency (IC_{50} = 5.75 μM) preserving its lead behavior and bio-potency compared to the standard reference used.

RSC Advances View Article Online DOI: 10.1039/C4RA16663A Paper

Table 1. Antitumor properties of the synthesized compounds **11-19**.

Entry	Compd.	R	R'	X	IC_{50}, μg/ml (μM)[a]	
					HeLa	HepG2
1	**11**	2,4-$Cl_2C_6H_3$	Et	H	10.27 (16.69)	2.17 (3.53)
2	**12**	2,4-$Cl_2C_6H_3$	Et	Cl	8.26 (12.71)	4.68 (7.20)
3	**13**	4-FC_6H_4	Et	H	2.50 (4.87)	5.60 (10.90)
4	**14**	4-FC_6H_4	Et	Cl	3.15 (5.75)	6.85 (12.50)
5	**15**	2-thienyl	Et	H	5.33 (10.89)	9.02 (18.42)
6	**16**	2-thienyl	Et	Cl	3.80 (7.25)	9.09 (17.34)
7	**17**	3-pyridinyl	Me	H	9.35 (20.08)	10.27 (22.06)
8	**18**	3-pyridinyl	Et	H	5.16 (10.76)	8.17 (17.04)
9	**19**	3-pyridinyl	Et	Cl	11.58 (22.53)	5.91 (11.50)
10	Doxorubicin hydrochloride	---	---	---	4.19 (7.22)	4.67 (8.05)
11	Cisplatin	---	---	---	4.19 (7.71)	3.58 (11.89)

[a]IC_{50} = concentration required to produce 50% inhibition of cell growth compared to control experimental.

Mapping of the HeLa 3D-pharmacophore with compound **13** (Figure S35 of supplementary material) describes the correlation of the pyrrolidinyl nitrogen with the positive ionizable feature. The same alignment was also observed for compound **11** (R = 2,4-$Cl_2C_6H_3$, R' = Et, X = H; IC_{50} = 16.69, 15.00 μM corresponding to the observed and estimated potency, respectively). The high potency difference between the observed/estimated activity of these compounds (**11, 13**) explains the role of the substituent attached to the phenyl group linked at the *C*-4' as explained previously in SAR due to the observed bio-data. The 2,4-dichlorophenyl group attached to *C*-4' position deactivates the positive ionizable properties of the pyrrolidinyl nitrogen much more than the *p*-fluorophenyl group (although the –I effect of fluorine is higher than chlorine, the two chlorine substituents combine to give a higher –I effect). The same applies for compound **16** (R = 2-thienyl, R' = Et, X = Cl; IC_{50} = 7.25, 10.42 μM corresponding to the observed and estimated potency, respectively) when compared with compound **19** (R = 3-pyridinyl, R' = Et, X = Cl; IC_{50} = 22.53, 22.04 μM corresponding to the observed and estimated potency, respectively). This latter observation correlates well with the electron donating properties of the thienyl group (five-membered heterocycle with one hetero atom) strengthen the positive ionizable property of pyrrolidinyl nitrogen upon compared with the effect of a 3-pyridinyl group (π-deficient heterocycle).

Mapping of the HepG2 3D-pharmacophore with compound **11** (R = 2,4-$Cl_2C_6H_3$, R' = Et, X = H; IC_{50} = 3.53, 4.26 μM corresponding to the observed and estimated potency, respectively), the most potent analogue among all the synthesized spiro-alkaloids (Figure S36 of supplementary material), describes the alignment of the 2,4-dichlorophenyl group attached to the pyrrolidinyl *C*-4' with the pharmacophoric hydrophobic feature and the pyrrolidinyl nitrogen with the pharmacophoric positive ionizable while the piperidinyl carbonyl is aligned with the hydrogen bond acceptor. A relatively similar mapping is exhibited by compound **13** (R = 4-FC_6H_4, R' = Et, X = H; IC_{50} = 10.90, 11.51 μM corresponding to the observed and estimated potency, respectively), where the 4-fluorophenyl group attached to the exocyclic olefinic linkage is aligned with the pharmacophoric hydrophobic feature, the pyrrolidinyl nitrogen with the positive ionizable, and the piperidinyl carbonyl is aligned with the hydrogen bond acceptor feature. The potency difference of compounds **11** and **13** can be attributed to the slight difference in mode of alignment and high hydrophobic properties of the 2,4-dichlorophenyl group aligned with the hydrophobic feature than the corresponding *p*-fluorophenyl group aligned with the same pharmacophoric feature. This observation is the same mentioned for SAR rules governing HepG2 bio-data. The potency decrease of compounds **12** (R = 2,4-$Cl_2C_6H_3$, R' = Et, X = Cl; IC_{50} = 7.20, 4.34 μM corresponding to the observed and estimated potency, respectively) and **14** (R = 4-FC_6H_4, R' = Et, X = Cl; IC_{50} = 12.50, 13.55 μM corresponding to the observed and estimated potency, respectively) "which exhibit typical alignment to compounds **11**, **13**, respectively" compared to their similar analogues **11** and **13** can be attributed to the effect of chloro substitution attached to the indolyl group which decreases the positive ionizable properties of the pyrrolidinyl nitrogen. Mapping of the HepG2 3D-pharmacophore with compound **18** (R = 3-pyridinyl, R' = Et, X = H; IC_{50} = 17.04, 18.90 μM corresponding to the observed and estimated potency, respectively), describes the alignment of the 3-pyridinyl group attached to the exocyclic olefinic linkage with the pharmacophoric hydrophobic, the pyrrolidinyl nitrogen with the positive ionizable, and the piperidinyl carbonyl with the hydrogen bond acceptor feature. A slightly modified mapping is observed for compound **15** (R = 2-thienyl, R' = Et, X = H; IC_{50} = 18.42, 19.15 μM corresponding to the observed and estimated potency, respectively) where, of the 2-thienyl group linked to the exocyclic olefinic linkage is aligned with the pharmacophoric hydrophobic, the pyrrolidinyl nitrogen with the positive ionizable, and the indolyl carbonyl with the hydrogen bond acceptor feature. The enhanced potency effect of compound **18** relative to compound **15** can be attributed not only to the slight difference in mode of alignment but also to the higher hydrophobic properties of the 3-pyridinyl group than the 2-thienyl function. Another reason for the observed pharmacological potency enhancement is extracted from the differences in mode of alignment where, the hydrogen bond

View Article Online
DOI: 10.1039/C4RA16663A
RSC Advances

acceptor property of the piperidinyl ketonic carbonyl is higher than that of indolyl carbonyl. Meanwhile, potency enhancement of compound **19** (R = 3-pyridinyl, R' = Et, X = Cl; IC_{50} = 11.50, 12.26 μM corresponding to the observed and estimated potency, respectively) compared with its similar analogue **18** is explained by the HepG2 pharmacophoric mapping of the former analogue in a completely different mode of alignment where, the chlorine substituent of the indolyl group is aligned with the pharmacophoric hydrophobic, the piperidinyl nitrogen with the positive ionizable, and the nitrogen of the 3-pyridinyl group linked at the *C*-4' is aligned with the hydrogen bond acceptor feature. The same applies also for compound **16** (R = 2-thienyl, R' = Et, X = Cl; IC_{50} = 17.34, 17.59 μM corresponding to the observed and estimated potency, respectively) that reveals a completely different mode of alignment in the hypothesized pharmacophore. Where the chlorine substituent of the indolyl group is aligned with the pharmacophoric hydrophobic, the piperidinyl nitrogen with the positive ionizable, and the indolyl carbonyl is aligned with the hydrogen bond acceptor feature. This is could be the reason for observed antitumor properties enhanced for compound **16** relative to its similar analogue **15**.

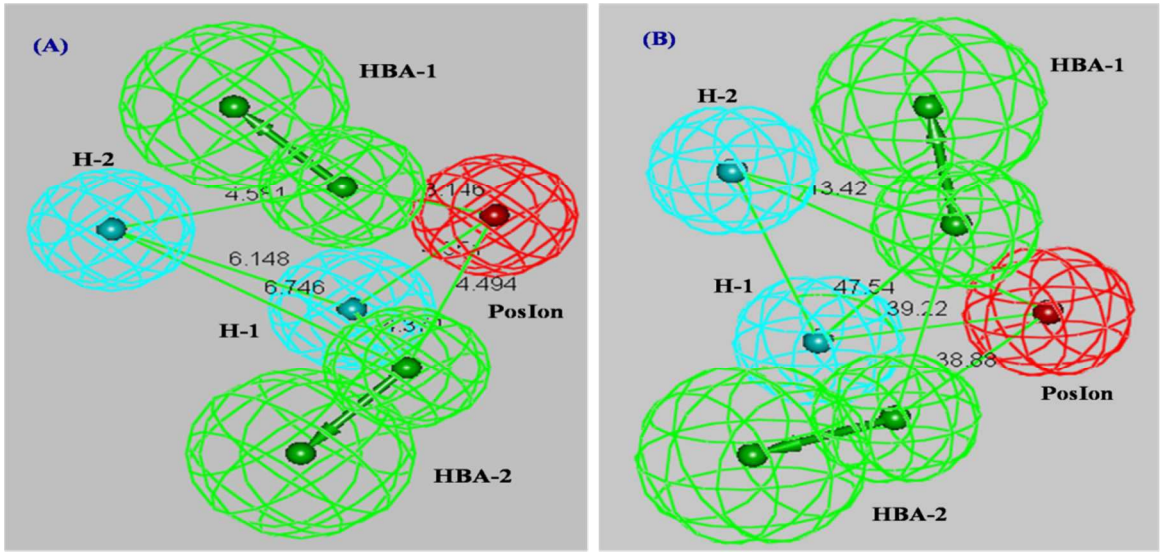

Figure 3 (**A**) Constraint distances and (**B**) constraint angles of the generated 3D-pharmacophore for the synthesized compounds **11-19** against HeLa (cervical) cell line which contains two hydrogen bonding acceptor (HBA-1, HBA-2, green), two hydrophobics (H-1, H-2, light blue), and one positive ionizable (PosIon, red).

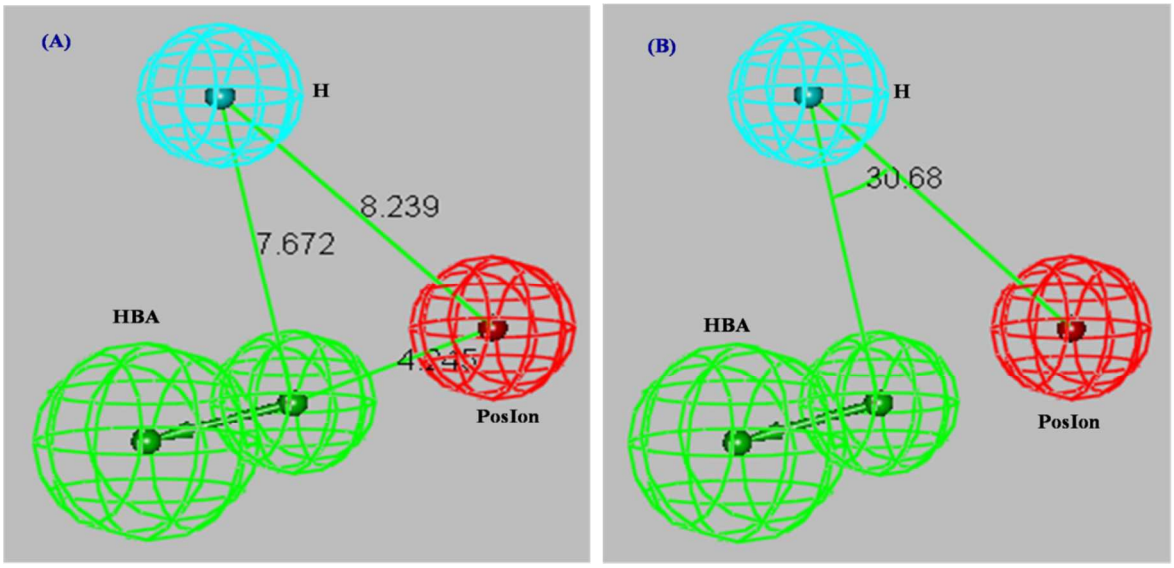

Figure 4 (**A**) Constraint distances and (**B**) constraint angles of the generated 3D-pharmacophore for the synthesized compounds **11-19** against HepG2 (liver) cell line which contains a hydrogen bonding acceptor (HBA, green), a hydrophobics (H, light blue), and a positive ionizable (PosIon, red).

RSC Advances
View Article Online
DOI: 10.1039/C4RA16663A Paper

Table 2 Constraint distances (Å) and angles (°) between features of the generated pharmacophores.

Cancer cell line	Constraint distances (Å)	Constraint angles (°)
HeLa (cervical)	(HBA-1)–(PosIon) = 3.146, (PosIon)–(H-1) = 4.551, (PosIon)–(HBA-2) = 4.494, (H-1)–(HBA-2) = 4.374, (HBA-2)–(H-2) = 6.746; (H-2)–(HBA-1) = 4.581, (H-1)–(H-2) = 6.148	(HBA-1)–(H-1)–(PosIon) = 39.22, (HBA-1)–(HBA-2)–(PosIon) = 38.88, (HBA-1)–(H-1)–(H-2) = 47.54, (HBA-1)–(H-2)–(PosIon) = 13.42
HepG2 (liver)	(H)–(PosIon) = 8.239, (PosIon)–(HBA) = 4.245, (HBA)–(H) = 7.672	(PosIon)–(H)–(HBA) = 30.68

Table 3. Best fit values and estimated/predicted activities for the synthesized compounds **11-19** mapped with the generated 3D-pharmacophore models due to HeLa (cervical) and HepG2 (liver) cancer cell lines.

Entry	Compd.	R	R'	X	HeLa (cervical) cell line			HepG2 (liver) cell line		
					Observed IC_{50}, μM	Estimated IC_{50}, μM	Fit value	Observed IC_{50}, μM	Estimated IC_{50}, μM	Fit value
1	**11**	2,4-$Cl_2C_6H_3$	Et	H	16.69	15.00	9.74	3.53	4.26	5.75
2	**12**	2,4-$Cl_2C_6H_3$	Et	Cl	12.71	10.65	9.88	7.20	4.34	5.74
3	**13**	4-FC_6H_4	Et	H	4.87	5.75	10.15	10.90	11.51	5.31
4	**14**	4-FC_6H_4	Et	Cl	5.75	7.02	10.07	12.50	13.55	5.24
5	**15**	2-thienyl	Et	H	10.89	11.05	9.87	18.42	19.15	5.09
6	**16**	2-thienyl	Et	Cl	7.25	10.42	9.89	17.34	17.59	5.13
7	**17**	3-pyridinyl	Me	H	20.08	14.69	9.74	22.06	21.71	5.04
8	**18**	3-pyridinyl	Et	H	10.76	9.47	9.94	17.04	18.90	5.10
9	**19**	3-pyridinyl	Et	Cl	22.53	22.04	9.57	11.50	12.26	5.29

2D-QSAR study

Data set

The basic idea behind QSAR is to generate a relationship between the chemical structure of an organic compound and its physico-chemical properties. Due to the limited pharmacologically active data set mentioned in the present study, external data points were considered. The external data points are derived from spiro-alkaloids having the same chemical scaffold (homogeneous/non-diverse data set protocol) and their bio-properties were determined by the same standard technique adopted in the present study. The QSAR study was undertaken using comprehensive descriptors for structural and statistical analysis (CODESSA-Pro) software employing the synthesized compounds of the present study **11,13,15-17,19** in addition to compounds **20-44** which are recently reported by our group[53] forming 31 spiro-alkaloids used as a training set for constructing QSAR models (Table 4). Compounds **12, 14,** and **18** (about one third of the synthesized analogues) representing high, and low potent antitumor active agents, were used as external data set for validating the attained QSAR models (Table 5).

Methodology

Geometry of the compounds was optimized using molecular mechanics force field (MM^+) followed by the semi-empirical AM1 method implemented in the HyperChem 8.0 package. The structures were fully optimized without fixing any parameters, thus bringing all geometric variables to their equilibrium values. The energy minimization protocol employed the Polake-Ribiere conjugated gradient algorithm. Convergence to a local minimum was achieved when the energy gradient was ≤0.01 kcal/mol. The RHF method was used in spin pairing for the two semi-empirical tools.[45,50,54,55] The resulting output files were exported to CODESSA-Pro that includes MOPAC capability for final geometry optimization. CODESSA-Pro software includes the following: (a) a calculation engine for more than 500 descriptors and (b) an engine for the development of the statistically most important linear and nonlinear QSAR regression models. CODESSA-Pro calculated 728 molecular descriptors including constitutional, topological, geometrical, charge-related, semi-empirical, molecular-type, atomic-type and bond-type descriptors for the exported 31 bio-active spiro-alkaloids **11,13,15-17,19**, and **20-44** which were used as a training set in the present study. Different mathematical transformations of the experimentally observed property/activity (IC_{50}, μM which is the concentration required to produce 50% inhibition of cell growth compared to control experimental) against HeLa (cervical) and HepG2 (liver) tumor cell lines of the training set compounds were utilized for the present QSAR modeling determination including property (IC_{50}, μM), 1/property, log(property) and 1/log(property) values in searching for the best QSAR models.

QSAR modeling

Best multi-linear regression (BMLR) was utilized which is a stepwise search for the best n-parameter regression equations (where, n stands for the number of descriptors used), based on the highest R^2 (squared correlation coefficient), R^2_{cv}OO (squared cross-validation "leave one-out, LOO" coefficient), R^2_{cv}MO (squared cross-validation "leave many-out, LMO" coefficient), F (Fisher statistical significance criteria) values, and s^2 (standard deviation). The QSAR models up to 3 and 4 descriptor models describing

Paper View Article Online DOI: 10.1039/C4RA16663A RSC Advances

bio-activity of the antitumor active agents against HeLa (cervical) and HepG2 (liver) cell line, respectively were generated (obeying the thumb rule of 5:1, which is the ratio between the data points and the number of QSAR descriptor models). Statistical characteristics of the QSAR models are presented in Tables 6, and 7. The established QSAR models are statistically significant. The descriptors are sorted in descending order of the respective values of the Student's t-criterion, which is a widely accepted measure of statistical significance of individual parameters in multiple linear regressions. Figures 5, and 6 exhibit the QSAR multi-linear model plot of correlations representing the observed *vs.* predicted IC_{50} values for HeLa and HepG2 tumor cell line active agents, respectively. The scattered plots are uniformly distributed, covering ranges, observed 0.688-1.387, 0.548-1.375; predicted 0.723-1.416, 0.574-1.328 logarithmic units for HeLa and HepG2 cell lines, respectively.

Molecular Descriptors

Molecular descriptors are the physic-chemical parameters used to correlate chemical structure and property value expressed as log(IC_{50}). The descriptors were obtained based on BMLR method. The descriptors controlling the bio-activity (property) by the established multi-linear QSAR models are presented in Tables 6, and 7 and are arranged, based on their level of significance (t-criterion).

HeLa (cervical) tumor cell line

The descriptors controlling bio-activity of the synthesized compounds against HeLa (cervical) tumor cell line according to the attained 3 descriptor QSAR model (Table 6) are: min. (#HA, #HD) (MOPAC PC), FNSA-2 fractional PNSA (PNSA-2/TMSA) (MOPAC PC), and HASA-2/SQRT(TMSA) (Zefirov PC) (all). The first descriptor controlling the HeLa QSAR model is minimum (#HA, #HD), which is a molecular type descriptor explaining the capability of the bio-active agent as hydrogen donor/acceptor. Although this descriptor is considered the most important one governing the attained QSAR model based on its t-criterion (9.200), its coefficient in the QSAR is the minimum among all the other observed QSAR descriptor (0.247). The second most important descriptor controlling the HeLa QSAR model based on the t-criterion (5.546) is FNSA-2 fractional PNSA (PNSA-2/TMSA), which is a charge related descriptor. The fractional total charge weighted partial negative surface area (FNSA2) is determined by equation (1).[56]

$$FNSA2=\frac{PNSA2}{TMSA} \quad \text{.....(1)}$$

where, *PNSA2* stands for total charge weighted partial negatively charged molecular surface area, and *TMSA* for total molecular surface area. This descriptor has the highest coefficient (0.596) among the other descriptors controlling the HeLa QSAR model. This observation coincide with our mentioned SAR rules governing bio-activity concerning type of substituent (halogen) attached to the phenyl group linked at the *C*-4' and consequently the exocyclic olefinic linkage, affecting greatly the observed potency of the bio-active agent. The same phenomenon is also extracted from the HeLa pharmacophoric hypothesis. The last descriptor of the HeLa QSAR model (t-criterion = 4.424), is HASA-2/SQRT(TMSA), which is also a charge related descriptor. The area-weighted surface charge of hydrogen bonding acceptor atoms (HASA2) is determined by equation (2).[56]

$$HASA2=\sum_A \frac{q_A\sqrt{S_A}}{\sqrt{S_{tot}}} A\in X_{H\text{-}acceptor} \quad \text{.....(2)}$$

where, S_A stands for solvent-accessible surface area of H-bonding acceptor atoms, q_A for partial charge on H-bonding acceptor atoms, and S_{tot} for total solvent-accessible molecular surface area. This descriptor is considered the second most effective parameter controlling the QSAR model based on its coefficient (0.426). The present descriptor also supported the attained SAR rules as explained in the previous descriptor (FNSA2).

HepGe (liver) tumor cell line

The attained HepG2 QSAR model exhibits 4 controlling descriptors (Table 7) which are: min. (#HA, #HD) (Zefirov PC), partial charged surface area for atom H, partial charged surface area for atom O, and min. (>0.1) bond order for atom C. The most important descript controlling the HepG2 QSAR model based on its t-criterion (7.157) is minimum (#HA, #HD) (Zefirov PC). This descriptor is a common for both HeLa and HepG2 QSAR models explaining its importance for the observed bio-properties in variable tumor cell lines. Although this descriptor is the most important one governing the HepG2 QSAR model, its coefficient is the minimum among all the other observed QSAR descriptor (0.152). The second and the third important descriptors of the HepG2 QSAR model are, partial charged surface area for atom H, and partial charged surface area for atom O, which are charge related descriptor. The partial positively or negatively charged surface area is determined by equation (3).[56]

$$PNSA1=\sum_A S_A A\in\{\delta_A< 0\} \quad \text{.....(3)}$$

where, S_A stands for positively or negatively charged solvent-accessible atomic surface area. The partial charged surface area for atom H descriptor participates in the HepG2 QSAR model with the greatest share among all the other descriptors (coefficient = 83.943). However, the partial charged surface area for atom O descriptor participated negatively in the HepG2 QSAR model (coefficient = -41.614), explaining that the higher of the latter descriptor value, the lower of total log(IC_{50}) observed, hence the higher potency of the constructed agent against HepG2 tumor cell line. This descriptor in particular can explain the potency of

RSC Advances View Article Online DOI: 10.1039/C4RA16663A Paper

compounds **11** (R = 2,4-$Cl_2C_6H_3$, R' = Et, X = H; IC_{50} = 3.53 μM) relative to **13** (R = 4-FC_6H_4, R' = Et, X = H; IC_{50} = 10.90 μM). This can be correlated with the halogen type/number substituted the phenyl group at *C*-4' and consequently the exocyclic olefinic linkage. The same observation was mentioned in the SAR rules governing bio-activity and 3D-pharmacophore modeling. The last descriptor of the HepG2 QSAR model is min. (>0.1) bond order for atom C, which is an atomic type descriptor.

Validation of QSAR model

Internal validation

The reliability and statistical relevance of the QSAR models are examined by internal and external validation procedures. Internal validation is applied by the CODESSA-Pro technique employing both Leave One Out (LOO), which involves developing a number of models with one example omitted at a time, and Leave Many Out (LMO), which involves developing a number of models with many data points omitted at a time (up to 20% of the total data points). The observed correlations due to the internal validation techniques are R^2cvOO = 0.738, 0.729; R^2cvMO = 0.776, 0.741, for HeLa and HepG2 QSAR models, respectively. Both of them are significantly correlated with the squared correlation coefficient of the attained QSAR models (R^2 = 0.815, 0.799 for HeLa and HepG2 QSAR models, respectively). Standard deviation of the regressions (s^2 = 0.008, 0.009 for HeLa and HepG2 QSAR models, respectively) is also a measurable value for the attained model together with the Fisher test value (F = 39.615, 25.768 for HeLa and HepG2 QSAR models, respectively) that reflects the ratio of the variance explained by the model and the variance due to their errors. A high value of F-test compared with the s^2 is a validation of the model. A randomization test was also performed in the present study which adds good support for the present QSAR models.

The predicted/estimated IC_{50} value of compound **13** (the most potent synthesized analogue among all the training set compounds) is 5.94 μM based on the HeLa QSAR model, matched with the experimentally observed value (4.87 μM, error "difference between observed and predicted values" = 1.07). All the other potent training set analogues (compounds **16,20-29,31,33-35,38**, and **42**) relative to cisplatin (standard reference clinically used against cervical carcinoma, IC_{50} = 7.71 μM) exhibit predicted IC_{50} values matched with their experimentally observed potency (error range = 0.06-1.12). Compounds **32**, and **39** which are also considered potent analogues against cervical carcimona (IC_{50} = 5.55, 5.51 μM corresponding to compounds **32**, and **39**, respectively) reveal relatively higher predicated potency beyond the mentioned error range (predicted IC_{50} = 7.78, 7.84 μM; error = 2.23, 2.33 corresponding to compounds **32**, and **39**, respectively). The mild antitumor active agents against HeLa cell line, compounds **15,30,37,41,43**, and **44** (IC_{50} range = 8.64-10.89 μM), reveal predicted potency (IC_{50} range = 6.27-10.77 μM) with relatively higher error range (0.41-2.47) than the high potent analogues. Additionally, the low potent analogues against HeLa cell lines, compounds **11,17,19,36**, and **40** (IC_{50} range = 11.20-24.36 μM) reveal higher deviated predicted potency (IC_{50} range = 6.53-26.07 μM) with error range = 1.64-5.99. From all the above statistical observations, the attained HeLa QSAR model can be considered a good predicative model with a powerful ability to produce high potent HeLa antitumor hits compared to those of mild or low potency. Actually, this is an acceptable observation where most of the training set compounds belong to the high potent HeLa antitumor agents (20 compounds out of 31, *i.e.* two thirds of the entire training set).

The predicted IC_{50} values (IC_{50} = 3.75-8.60 μM) of the potent HepG2 analogues **11,20-24,26,28,29,31-35,** and **37-39** (IC_{50} = 3.53-7.49 μM) relative to doxorubicin hydrochloride (IC_{50} = 8.05 μM standard reference used in the present study "clinically used as liver antitumor agent") exhibit error range = 0.08-1.92. However, wilder error range was observed for the mild HepG2 antitumor agents, compounds **25,27,** and **42-44** (IC_{50} = 8.73-9.37, 6.32-11.04 μM, corresponding to the observed and predicted values, respectively, error range = 0.17-2.57) and low HepG2 antitumor agents, compounds **13,15-17,19,30,36,40,** and **41** (IC_{50} = 10.90-23.71, 7.63-21.29 μM, corresponding to the observed and predicted values, respectively, error range = 0.37-5.31). This is an indication for the ability of utilization of the attained HepG2 QSAR model for optimizing high potent HepG2 (liver) antitumor agents than either mild or low effective hits. The reason for this observation can be attributed as mentioned in the former HeLa QSAR model, due to participation of high number of potent agents compared to mild and low potent analogues (14 out of 31 analogous of the training set *i.e.* 45%).

External validation

Compounds **12, 14,** and **18** were used as an external test set not only for validating the attained QSAR models but also for examining their predicative ability. The test set analogues experimentally exhibit high and low potency against the tested cell lines. The variation in potency can indicate the predication capabilities of the QSAR models. Table 5 reveals the observed and predicted IC_{50} values of the test set compounds. From the observed data, it has been noticed that compound **14** which is considered a high potent agent against HeLa cell line (IC_{50} = 5.75 μM), relative to cisplatin, standard reference used, reveals a predicted IC_{50} = 5.64 μM with minimum error value = 0.11. Compounds **12,** and **18** that considered low potent analogues (IC_{50} = 12.71, 10.76 μM, respectively), afforded predicted IC_{50} = 8.99, 23.70 μM, respectively (error values = 3.72, 12.94, respectively).

View Article Online
DOI: 10.1039/C4RA16663A

RSC Advances

RSCPublishing

PAPER

Table 4 Observed and predicated values of training set compounds **11,13,15-17,** and **19-44** according to the multi-linear QSAR models.

Entry	Compd.	R	R'	X	HeLa (cervical) cell line			HepG2 (liver) cell line		
					Observed IC_{50}, μM	Estimated IC_{50}, μM	Error	Observed IC_{50}, μM	Estimated IC_{50}, μM	Error
1	**11**	2,4-$Cl_2C_6H_3$	Et	H	16.69	12.26	4.43	3.53	3.75	-0.22
2	**13**	4-FC_6H_4	Et	H	4.87	5.94	-1.07	10.90	7.63	3.27
3	**15**	2-thienyl	Et	H	10.89	10.48	0.41	18.42	15.69	2.73
4	**16**	2-thienyl	Et	Cl	7.25	7.86	-0.61	17.34	16.97	0.37
5	**17**	3-pyridinyl	Me	H	20.08	26.07	-5.99	22.06	21.29	0.77
6	**19**	3-pyridinyl	Et	Cl	22.53	20.89	1.64	11.50	16.32	-4.82
7	**20**	Ph	Me	H	6.21	5.92	0.29	7.46	8.34	-0.88
8	**21**	Ph	Me	Cl	5.92	5.41	0.51	5.66	6.16	-0.50
9	**22**	4-ClC_6H_4	Me	H	6.74	6.30	0.44	6.03	6.13	-0.10
10	**23**	4-ClC_6H_4	Me	Cl	5.08	5.72	-0.64	6.26	6.34	-0.08
11	**24**	4-ClC_6H_4	Et	Cl	4.96	5.28	-0.32	5.73	5.81	-0.08
12	**25**	4-ClC_6H_4	Me	OMe	5.78	5.90	-0.12	8.89	6.32	2.57
13	**26**	4-ClC_6H_4	Et	OMe	5.20	5.43	-0.23	5.43	5.33	0.10
14	**27**	4-FC_6H_4	Me	H	6.51	5.95	0.56	8.73	8.90	-0.17
15	**28**	4-FC_6H_4	Me	Cl	5.15	5.71	-0.56	5.77	7.41	-1.64
16	**29**	4-FC_6H_4	Me	OMe	5.44	6.21	-0.77	5.82	6.31	-0.49
17	**30**	4-$H_3CC_6H_4$	Me	H	8.64	7.09	1.55	14.18	8.87	5.31
18	**31**	4-$H_3CC_6H_4$	Me	Cl	6.65	6.71	-0.06	7.32	6.67	0.65
19	**32**	4-$H_3CC_6H_4$	Et	Cl	5.55	7.78	-2.23	5.46	7.14	-1.68
20	**33**	4-$H_3CC_6H_4$	Me	OMe	6.96	7.68	-0.72	6.15	6.36	-0.21
21	**34**	4-$H_3COC_6H_4$	Me	H	6.45	7.17	-0.72	6.68	8.60	-1.92
22	**35**	4-$H_3COC_6H_4$	Et	H	7.22	6.54	0.68	6.68	7.21	-0.53
23	**36**	4-$H_3COC_6H_4$	Me	Cl	11.20	6.53	4.67	13.67	8.36	5.31
24	**37**	4-$H_3COC_6H_4$	Et	Cl	8.74	6.27	2.47	5.91	8.05	-2.14
25	**38**	4-$H_3COC_6H_4$	Me	OMe	6.10	6.94	-0.84	6.95	7.35	-0.40
26	**39**	4-$H_3COC_6H_4$	Et	OMe	5.51	7.84	-2.33	7.49	7.35	0.14
27	**40**	4-$Me_2NC_6H_4$	Me	Cl	24.36	20.24	4.12	23.71	21.13	2.58
28	**41**	2-thienyl	Me	H	8.94	8.18	0.76	14.02	13.76	0.26
29	**42**	2-thienyl	Me	Cl	6.86	7.98	-1.12	9.29	11.04	-1.75
30	**43**	2-thienyl	Me	OMe	9.65	10.77	-1.12	8.40	7.07	1.33
31	**44**	5-methyl-2-furanyl	Me	Cl	9.88	8.46	1.42	9.37	10.81	-1.44

Table 5 Observed and predicated values of external test set compounds **12, 14,** and **18** according to the multi-linear QSAR models.

Entry	Compd.	R	R'	X	HeLa (cervical) cell line			HepG2 (liver) cell line		
					Observed IC_{50}, μM	Estimated IC_{50}, μM	Error	Observed IC_{50}, μM	Estimated IC_{50}, μM	Error
1	**12**	2,4-$Cl_2C_6H_3$	Et	Cl	12.71	8.99	3.72	7.20	4.03	3.17
2	**14**	4-FC_6H_4	Et	Cl	5.75	5.64	0.11	12.50	8.00	4.50
3	**18**	3-pyridinyl	Et	H	10.76	23.70	-12.94	17.04	16.97	0.07

Table 6 Descriptor of the best multi-linear QSAR model for the HeLa (cervical) tumor cell line active agents.

Entry	N=31, n=3, R^2=0.815, R^2cvOO=0.738, R^2cvMO=0.776, F=39.615, s^2=0.008				
	ID	coefficient	s	t	Descriptor
1	0	0.141	0.185	0.763	Intercept
2	D_1	0.247	0.027	9.200	Min.(#HA, #HD) (MOPAC PC)
3	D_2	0.596	0.107	5.546	FNSA-2 Fractional PNSA (PNSA-2/TMSA) (MOPAC PC)
4	D_3	0.426	0.096	4.424	HASA-2/SQRT(TMSA) (Zefirov PC) (all)

$\log(IC_{50}) = 0.141 + (0.247 \times D_1) + (0.596 \times D_2) + (0.426 \times D_3)$

RSC Advances
View Article Online
DOI: 10.1039/C4RA16633J
Paper

Table 7 Descriptor of the best multi-linear QSAR model for the HepG2 (liver) tumor cell line active agents.

Entry	N=31, n=4, R^2=0.799, R^2cvOO=0.729, R^2cvMO=0.741, F=25.768, s^2=0.009				
	ID	coefficient	s	t	Descriptor
1	0	5.211	1.493	3.491	Intercept
2	D_1	0.152	0.021	7.157	Min.(#HA, #HD) (Zefirov PC)
3	D_2	83.943	17.380	4.830	Partial Charged Surface Area for atom H
4	D_3	-41.614	8.822	-4.717	Partial Charged Surface Area for atom O
5	D_4	-60.210	14.595	-4.125	Min. (>0.1) bond order for atom C
$\log(IC_{50}) = 5.211 + (0.152 \times D_1) + (83.943 \times D_2) - (41.614 \times D_3) - (60.210 \times D_4)$					

These observations give good sign for the predictive capability of the attained HeLa QSAR model and support the previous statement concerning its predictive power due to the statistical values.

Predicted value for compound **12,** IC_{50} = 4.03 μM, is correlated to its high potency against HepG2 cell line (observed IC_{50} = 7.20 μM). Although the error value due to difference between the observed and predicted IC_{50} values is considered a relatively high (error value = 3.17), the observed potency of the analogue is still preserved relative to doxorubicin hydrochloride, standard reference used (IC_{50} = 8.05 μM). Compounds **14,** and **18** which are considered low potent HepG2 antitumor agents (observed IC_{50} = 12.50, 17.04 μM, respectively) reveal predicted IC_{50} values = 8.00, 16.97 μM, respectively (error values = 4.50, 0.07, respectively). The overall observations due to test set predication values give a good indication for the predictive power of the attained QSAR models for optimizing high potent hits having spiro-alkaloid scaffold.

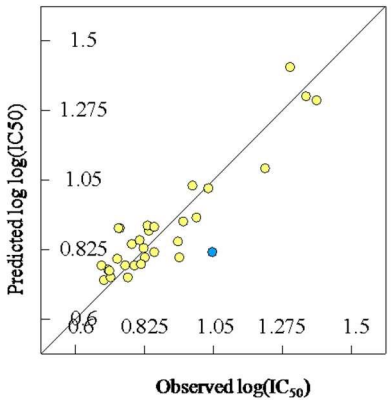

Figure 5 QSAR best multi-linear model plot of correlations representing the observed *vs.* predicted IC_{50} values for HeLa (cervical) tumor cell line active agents (compound **36** is an outlier).

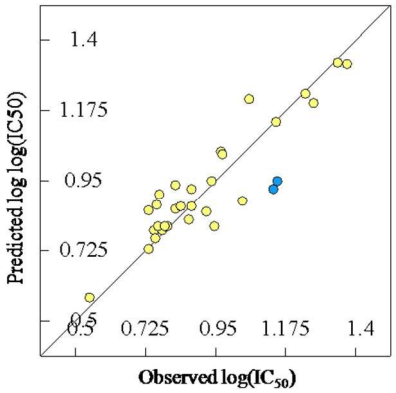

Figure 6 QSAR best multi-linear model plot of correlations representing the observed *vs.* predicted IC_{50} values for HepG2 (liver) tumor cell line active agents (compounds **30**, and **36** are outliers).

Conclusion

[3+2]-Cycloaddition reactions of non-stabilized azomethine ylide (generated *in situ via* decarboxylative condensation of isatins **8,9** with sarcosine **10**) and 3*E*,5*E*-1-alkyl-3,5-bis(arylmethylidene)-4-piperidones **3-7** afforded 1''-alkyl-4'-aryl-5''-(arylmethylidene)-1'-methyl-dispiro[3*H*-indole-3,2'-pyrrolidine-3',3''-piperidine]-2(1*H*),4''-diones **11-19** in regioselective manner. Compounds **13**, **14**, and **16** reveal higher potency against HeLa (cervical) cell line than the standard reference cisplatin, while compounds **11**, and **12** seem more potent than doxorubicin hydrochloride (clinically applicable agent against liver carcinoma) through *in-vitro* Sulfo-Rhodamine-B bio-assay. 3D-pharmacophore study utilizing Discovery Studio 2.5 software explained the antitumor variability of the tested compounds based on chemical structural features. The HeLa pharmacophore contains five chemical features; two hydrogen bond acceptors, two hydrophobics, and one positive ionizable. The HepG2 pharmacophore comprises three chemical features; a hydrogen bond acceptor, a hydrophobic, and a positive ionizable. 2D-QSAR study was undertaken utilizing CODESSA-Pro software in order to validate the antitumor observed bio-data and determine the most important parameters controlling bio-activity. Statistically significant robust QSAR models describing the spiro-alkaloids bio-properties were obtained. External validation technique

View Article Online
DOI: 10.1039/C4RA16693A
RSC Advances

utilizing high and low potent synthesized agents, support the predictive power of the attained QSAR models. Homogeneity of the training set analogues (the same chemical scaffold) may be the main factor for the success of the QSAR models.

Experimental

Melting points were determined on a capillary tube digital Stuart SMP3 melting point apparatus. IR spectra (KBr) were recorded on a JASCO 6100 FT-IR spectrophotometer. NMR spectra were recorded on Mercury or Gemini NMR spectrometers operating at 300 MHz for ^{1}H (with TMS as an internal standard) and 75 MHz for ^{13}C, except ^{13}C-NMR spectra of compounds **17-19** which were recorded on a Bruker Ascend 400/R (100 MHz) spectrometer. High-resolution mass spectra (HRMS) were recorded on an Agilent Technologies 6210 Time of Flight LC/MS instrument operating in the ESI mode. The starting compounds **4-7** were prepared according to the reported procedures.[57–59]

Synthesis of 3*E*,5*E*-3,5-bis[(2,4-dichlorophenyl)methylidene]-1-ethyl-4-piperidone (3). A mixture of 1-ethyl-4-piperidone **2** (0.64 ml, 5 mmol), and 2,4-dichlorobenzaldehyde (1.75 g, 10 mmol) in 10 ml methanol containing KOH (0.56 g, 10 mmol), was stirred at room temperature (25 °C) for 3 h. The separated solid after storing the reaction mixture overnight at room temperature, was collected, washed with water, and crystallized from n-butanol affording **3** as pale yellow microcrystals, mp 136-138 °C (lit. mp 100.4–103.7 °C)[50], yield 1.95 g (88%). IR: ν_{max}/cm^{-1} 1674 (C=O), 1616, 1584. ^{1}H-NMR ($CDCl_3$) (300 MHz): δ 0.99 (t, J = 7.2 Hz, 3H, NCH$_2$*CH$_3$*), 2.53 (q, J = 7.2 Hz, 2H, N*CH$_2$*CH$_3$), 3.64 (s, 4H, piperidinyl 2N*CH$_2$*), 7.17 (d, J = 8.3 Hz, 2H, arom. *H*-6/6'), 7.29 (td, J = 8.3, 3.4, 1.7 Hz, Hz, 2H, arom. *H*-5/5'), 7.47 (t, J = 1.7 Hz, 2H, arom. *H*-3/3'), 7.91 (s, 2H, olefinic H's). ^{13}C-NMR ($CDCl_3$) (75 MHz): δ 12.4 (piperidinyl NCH$_2$*C*H$_3$), 51.0 (piperidinyl NCH$_2$CH$_3$), 54.0 [piperidinyl NCH$_2$ (*C*-2/6)], 127.1 (arom. *C*-5'), 130.1 (arom. *C*-3'), 131.1 (arom. *C*-6'), 132.2 (arom. *C*-4'), 133.2 (arom. *C*-1'), 134.8 (arom. *C*-2'), 135.5 (piperidinyl *C*-3/5), 136.1 (olefinic *C*H), 186.3 [piperidinyl *C*-4 (C=O)]. Anal. Calcd. for $C_{21}H_{17}Cl_4NO$ (441.19): C, 57.17; H, 3.88; N, 3.17. Found: C, 57.33; H, 3.56; N, 2.97.

Synthesis of 1''-alkyl-4'-aryl-5''-(arylmethylidene)-1'-methyl-dispiro[3*H*-indole-3,2'-pyrrolidine-3',3''-piperidine]-2(1*H*),4''-diones 11-19 (General procedure): A mixture of equimolar amounts of the appropriate 1-alkyl-3,5-bis(arylmethylidene)-4-piperidones **3-7** (2 mmol), the corresponding isatins **8,9** and sarcosine **10** in absolute ethanol (10 ml) was heated under reflux for the appropriate time. The separated solid while refluxing was collected and crystallized from suitable solvent affording compounds **11-13,15,16,** and **19**. In the case of **14**, the clear reaction mixture was stored at room temperature overnight. The separated solid was collected and crystallized from a suitable solvent. In case of **17**, and **18**, the reaction mixture was evaporated till dryness. The separated solid upon triturating the residue with methanol (5 ml) was collected and crystallized from a suitable solvent.

4'-(2,4-Dichlorophenyl)-5''-[(2,4-dichlorophenyl)methylidene]-1''-ethyl-1'-methyl-dispiro[3*H*-indole-3,2'-pyrrolidine-3',3''-piperidine]-2(1*H*),4''-dione (11). Obtained from reaction of **3**, **8** and **10**. Reaction time 12 h, pale yellow microcrystals from *n*-butanol, mp 232-234 °C, yield 1.07 g (87%). IR: ν_{max}/cm^{-1} 3285 (NH), 1701, 1678 (C=O), 1611, 1601. ^{1}H-NMR (DMSO-d_6) (300 MHz): δ 0.67 (t, J = 7.1 Hz, 3H, NCH$_2$*CH$_3$*), 1.71 (d, J = 12.5 Hz, 1H, upfield H of piperidinyl *H$_2$C*-2''), 1.92 (s, 3H, pyrrolidinyl N*CH$_3$*), 1.93-2.11 (m, 2H, piperidinyl N*CH$_2$*CH$_3$), 2.91 (d, J = 12.8 Hz, 1H, downfield H of piperidinyl *H$_2$C*-2''), 3.10 (d, J = 15.4 Hz, 1H, upfield H of piperidinyl *H$_2$C*-6''), 3.28-3.40 (m, 2H, downfield H of piperidinyl *H$_2$C*-6'' + upfield H of pyrrolidinyl *H$_2$C*-5), 3.77 (t, J = 9.0 Hz, 1H, downfield H of pyrrolidinyl *H$_2$C*-5'), 4.89 (t, J = 8.7 Hz, 1H, pyrrolidinyl *HC*-4'), 6.65 (d, J = 7.6 Hz, 1H, arom. H), 6.82-6.84 (m, 2H, arom. H), 7.04-7.08 (m, 1H, arom. H), 7.11 (d, J = 8.3 Hz, 1H, arom. H), 7.34 (dd, J = 8.4, 2.1 Hz, 1H, arom. H), 7.42 (s, 1H, olefinic *CH*), 7.47-7.51 (m, 2H, arom. H), 7.61 (d, J = 2.2 Hz, 1H, arom. H), 7.98 (d, J = 8.5 Hz, 1H, arom. H), 10.57 (s, 1H, NH). ^{13}C-NMR (DMSO-d_6) (75 MHz): δ 11.0 (piperidinyl NCH$_2$*C*H$_3$), 33.9 (pyrrolidinyl N*C*H$_3$), 41.3 (pyrrolidinyl H*C*-4'), 51.4 (piperidinyl N*C*H$_2$CH$_3$), 53.4 (piperidinyl H$_2$*C*-6''), 56.1 (piperidinyl H$_2$*C*-2''), 57.0 (pyrrolidinyl H$_2$*C*-5'), 62.1[spiro *C*-3' (*C*-3'')], 76.2 [spiro *C*-3 (*C*-2')], 108.8, 121.2, 125.9, 127.1, 127.2, 128.4, 129.1, 131.2, 131.5, 132.0, 132.1, 134.1, 134.7, 134.8, 135.6, 135.8, 143.6 (arom. *C* + olefinic *C*), 176.3 [indolyl *C*=O (*C*-2)], 196.8 [piperidinyl *C*=O (*C*-4'')]. Anal. Calcd. for $C_{31}H_{27}Cl_4N_3O_2$ (615.39): C, 60.50; H, 4.42; N, 6.83. Found: C, 60.89; H, 4.50; N, 6.46.

5-Chloro-4'-(2,4-dichlorophenyl)-5''-[(2,4-dichlorophenyl)methylidene]-1''-ethyl-1'-methyl-dispiro[3*H*-indole-3,2'-pyrrolidine-3',3''-piperidine]-2(1*H*),4''-dione (12). Obtained from reaction of **3**, **9** and **10**. Reaction time 12 h, pale yellow microcrystals from methanol, mp 203-204 °C, yield 0.81 g (62%). IR: ν_{max}/cm^{-1} 3414 (NH), 1721, 1694 (C=O), 1607, 1585. ^{1}H-NMR (DMSO-d_6) (300 MHz): δ 0.68 (t, J = 7.1 Hz, 3H, piperidinyl NCH$_2$*CH$_3$*), 1.72 (d, J = 12.5 Hz, 1H, upfield H of piperidinyl *H$_2$C*-2''), 1.94 (s, 3H, pyrrolidinyl N*CH$_3$*), 1.98-2.13 (m, 2H, piperidinyl N*CH$_2$*CH$_3$), 2.95 (d, J = 12.6 Hz, 1H, downfield H of piperidinyl *H$_2$C*-2''), 3.15 (d, J = 13.6 Hz, 1H, upfield H of piperidinyl *H$_2$C*-6''), 3.29-3.35 (m, 2H, downfield H of piperidinyl *H$_2$C*-6'' + upfield H of pyrrolidinyl *H$_2$C*-5'), 3.75 (t, J = 9.1 Hz, 1H, downfield H of pyrrolidinyl *H$_2$C*-5'), 4.83 (t, J = 8.6 Hz, 1H, pyrrolidinyl *HC*-4'), 6.69 (d, J = 8.3 Hz, 1H, arom. H), 6.78 (d, J = 2.0 Hz, 1H, arom. H), 7.16 (dd, J = 8.2, 2.2 Hz, 1H, arom, H), 7.18 (s, 1H, arom. H), 7.37 (dd, J = 8.4, 1.9 Hz, 1H, arom. H), 7.43 (s, 1H, olefinic *CH*), 7.49-7.53 (m, 2H, arom. H), 7.63 (d, J = 2.1 Hz, 1H, arom. H), 7.91 (d, J = 8.5 Hz, 1H,

RSC Advances View Article Online DOI: 10.1039/C4RA16663A Paper

arom. H), 10.73 (s, 1H, NH). ^{13}C-NMR (DMSO-d_6) (75 MHz): δ 11.0 (piperidinyl NCH$_2$*C*H$_3$), 34.0 (pyrrolidinyl N*C*H$_3$), 41.6 (pyrrolidinyl H*C*-4'), 51.4 (piperidinyl N*C*H$_2$CH$_3$), 53.3 (piperidinyl H$_2$*C*-6"), 56.1 (piperidinyl H$_2$*C*-2"), 57.0 (pyrrolidinyl H$_2$*C*-5'), 62.7 [spiro *C*-3' (*C*-3")], 76.1 [spiro *C*-3 (*C*-2')], 110.4, 125.4, 126.7, 127.2, 127.3, 128.2, 128.5, 128.6, 129.2, 131.2, 131.5, 131.9, 132.2, 134.3, 134.5, 134.7, 135.5, 135.6, 142.5 (arom. *C* + olefinic *C*), 176.0 [indolyl *C*=O (*C*-2)], 196.8 [piperidinyl *C*=O (*C*-4")]. Anal. Calcd. for $C_{31}H_{26}Cl_5N_3O_2$ (649.84): C, 57.30; H, 4.03; N, 6.47. Found: C, 57.67; H, 3.77; N, 6.30.

1"-Ethyl-4'-(4-fluorophenyl)-5"-[(4-fluorophenyl)methylidene]-1'-methyl-dispiro[3*H*-indole-3,2'-pyrrolidine-3',3"-piperidine]-2(1*H*),4"-dione (13). Obtained from reaction of **4**, **8** and **10**. Reaction time 6 h, colorless microcrystals from n-butanol, mp 219-221 °C, yield 1.01 g (98%). IR: ν_{max}/cm^{-1} 3198 (NH), 1686 (C=O), 1611, 1601. ^{1}H-NMR (DMSO-d_6) (300 MHz): δ 0.74 (t, J = 7.1 Hz, 3H, piperidinyl NCH$_2$*CH*$_3$), 1.63 (d, J = 12.4 Hz, 1H, upfield H of piperidinyl *H*$_2$*C*-2"), 1.94 (s, 3H, pyrrolidinyl N*CH*$_3$), 2.02-2.13 (m, 1H, upfield H of piperidinyl N*CH*$_2$CH$_3$), 2.17-2.28 (m, 1H, downfield H of piperidinyl N*CH*$_2$CH$_3$), 2.90 (dd, J = 14.9, 2.5 Hz, 1H, upfield H of piperidinyl *H*$_2$*C*-6"), 3.09-3.32 (m, 3H, downfield H of piperidinyl *H*$_2$*C*-2" + downfield H of piperidinyl *H*$_2$*C*-6" + upfield H of pyrrolidinyl *H*$_2$*C*-5'), 3.75 (t, J = 9.6 Hz, 1H, downfield H of pyrrolidinyl *H*$_2$*C*-5'), 4.61 (dd, J = 10.7, 7.4 Hz, 1H, pyrrolidinyl *HC*-4'), 6.56-7.36 (m, 13H, 12 arom. H + olefinic *CH*), 10.35 (s, 1H, NH).^{13}C-NMR (DMSO-d_6) (75 MHz): δ 10.9 (piperidinyl NCH$_2$*C*H$_3$), 34.0 (pyrrolidinyl N*C*H$_3$), 44.4 (pyrrolidinyl H*C*-4'), 51.1 (piperidinyl N*C*H$_2$CH$_3$), 53.2 (piperidinyl H$_2$*C*-6"), 56.0 (piperidinyl H$_2$*C*-2"), 56.6 (pyrrolidinyl H$_2$*C*-5'), 64.1 [spiro *C*-3' (*C*-3")], 75.3 [spiro *C*-3 (*C*-2')], 108.6, 114.8, 115.1, 115.4, 115.6, 120.6, 126.7, 126.9, 128.5, 130.9, 131.0, 131.1, 131.12, 132.3, 132.4, 132.9, 134.6, 134.63, 135.5, 143.4, 159.5, 160.4, 162.7, 163.7 (arom. *C* + olefinic *C*), 176.5 [indolyl *C*=O (*C*-2)], 198.2 [piperidinyl *C*=O (*C*-4")]. HRMS (ESI): *m/z* [M + H]$^+$ calcd for $C_{31}H_{29}F_2N_3O_2$: 514.2301,found: 514.2326.

5-Chloro-1"-ethyl-4'-(4-fluorophenyl)-5"-[(4-fluorophenyl)methylidene]-1'-methyl-dispiro[3*H*-indole-3,2'-pyrrolidine-3',3"-piperidine]-2(1*H*),4"-dione (14). Obtained from reaction of **4**, **9** and **10**. Reaction time 10 h, pale yellow microcrystals from methanol, mp 210-212 °C, yield 0.80 g (73%). IR: ν_{max}/cm^{-1} 3157 (NH), 1701, 1678 (C=O), 1599, 1585. ^{1}H-NMR (DMSO-d_6) (300 MHz): δ 0.76 (t, J = 7.1 Hz, 3H, piperidinyl NCH$_2$*CH*$_3$), 1.64 (d, J = 12.5 Hz, 1H, upfield H of piperidinyl *H*$_2$*C*-2"), 1.98 (s, 3H, pyrrolidinyl N*CH*$_3$), 2.06-2.14 (m, 1H, upfield H of piperidinyl N*CH*$_2$CH$_3$), 2.18-2.30 (m, 1H, downfield H of piperidinyl N*CH*$_2$CH$_3$), 2.95 (d, J = 13.9 Hz, 1H, upfield H of piperidinyl *H*$_2$*C*-6"), 3.10-3.34 (m, 3H, downfield H of piperidinyl *H*$_2$*C*-2" + downfield H of piperidinyl *H*$_2$*C*-6" + upfield H of pyrrolidinyl *H*$_2$*C*-5'), 3.74 (t, J = 9.7 Hz, 1H, downfield H of pyrrolidinyl *H*$_2$*C*-5'), 4.62 (dd, J = 10.7, 7.5 Hz, 1H, pyrrolidinyl *HC*-4'), 6.59-7.37 (m, 12H, 11 arom. H + olefinic *CH*), 10.55 (s, 1H, NH). ^{13}C-NMR (DMSO-d_6) (75 MHz): δ 10.9 (piperidinyl NCH$_2$*C*H$_3$), 34.1 (pyrrolidinyl N*C*H$_3$), 44.2 (pyrrolidinyl H*C*-4'), 51.1 (piperidinyl N*C*H$_2$CH$_3$), 53.2 (piperidinyl H$_2$*C*-6"), 56.1 (piperidinyl H$_2$*C*-2"), 56.7 (pyrrolidinyl H$_2$*C*-5'), 64.5 [spiro *C*-3' (*C*-3")], 75.3 [spiro *C*-3 (*C*-2')], 110.1, 114.9, 115.1, 115.5, 115.8, 124.8, 126.7, 128.4, 128.9, 130.8, 130.9, 131.0, 132.3, 132.4, 132.92, 132.94, 134.3, 134.31, 135.9, 142.4, 159.5, 160.5, 162.7, 163.8 (arom. *C* + olefinic *C*), 176.1 [indolyl *C*=O (*C*-2)], 198.0 [piperidinyl *C*=O (*C*-4")]. HRMS (ESI): *m/z* [M + H]$^+$ calcd for $C_{31}H_{29}ClF_2N_3O_2$: 548.1911, found: 548.1902.

1"-Ethyl-1'-methyl-4'-(2-thienyl)-5"-[(2-thienyl)methylidene]-dispiro[3*H*-indole-3,2'-pyrrolidine-3',3"-piperidine]-2(1*H*),4"-dione (15). Obtained from reaction of **5**, **8** and **10**. Reaction time 9 h, yellow microcrystals from *N,N*-dimethylformamide, mp 236-237 °C, yield 0.84 g (86%). IR: ν_{max}/cm^{-1} 3198 (NH), 1694, 1676 (C=O), 1614, 1576. ^{1}H-NMR (DMSO-d_6) (300 MHz): δ 0.86 (t, J = 6.9 Hz, 3H, piperidinyl NCH$_2$*CH*$_3$), 1.86 (d, J = 12.3 Hz, 1H, upfield H of piperidinyl *H*$_2$*C*-2"), 1.94 (s, 3H, pyrrolidinyl N*CH*$_3$), 2.12-2.19 (m, 1H, upfield H of piperidinyl N*CH*$_2$CH$_3$), 2.34-2.42 (m, 1H, downfield H of piperidinyl N*CH*$_2$CH$_3$), 2.83 (d, J = 15.1 Hz, 1H, upfield H of piperidinyl *H*$_2$*C*-6"), 3.23-3.33 (m, 3H, downfield H of piperidinyl *H*$_2$*C*-2" + downfield H of piperidinyl *H*$_2$*C*-6" + upfield H of pyrrolidinyl *H*$_2$*C*-5'), 3.77 (t, J = 9.7 Hz, 1H, downfield H of pyrrolidinyl *H*$_2$*C*-5'), 4.87 (t, J = 8.9 Hz, 1H, pyrrolidinyl *HC*-4'), 6.62 (d, J = 7.8 Hz, 1H, arom. H), 6.70 (t, J = 7.4 Hz, 1H, arom. H), 6.79-7.61 (m, 8H, 7 arom H + olefinic *CH*), 7.81 (d, J = 4.5 Hz, 1H, arom. H), 10.38 (s, 1H, NH). ^{13}C-NMR (DMSO-d_6) (75 MHz): δ 11.0 (piperidinyl NCH$_2$*C*H$_3$), 33.8 (pyrrolidinyl N*C*H$_3$), 40.2 (pyrrolidinyl H*C*-4'), 51.4 (piperidinyl N*C*H$_2$CH$_3$), 53.1 (piperidinyl H$_2$*C*-6"), 54.8 (piperidinyl H$_2$*C*-2"), 57.5 (pyrrolidinyl H$_2$*C*-5'), 63.7 [spiro *C*-3' (*C*-3")], 75.3 [spiro *C*-3 (*C*-2')], 108.5, 120.4, 124.4, 126.0, 126.6, 126.9, 128.3, 128.8, 129.3, 132.2, 134.0, 137.6, 141.0, 143.6 (arom. *C* + olefinic *C*), 176.3 [indolyl *C*=O (*C*-2)], 196.5 [piperidinyl *C*=O (*C*-4")]. HRMS (ESI): *m/z* [M + H]$^+$ calcd for $C_{27}H_{27}N_3O_2S_2$: 490.1617,found: 490.1640.

5-Chloro-1"-ethyl-1'-methyl-4'-(2-thienyl)-5"-[(2-thienyl)methylidene]-dispiro[3*H*-indole-3,2'-pyrrolidine-3',3"-piperidine]-2(1*H*),4"-dione (16). Obtained from reaction of **5**, **9** and **10**. Reaction time 11 h, pale yellow microcrystals from *n*-butanol, mp 226-228 °C, yield 0.88 g (84%). IR: ν_{max}/cm^{-1} 3183 (NH), 1695, 1672 (C=O), 1618, 1574. ^{1}H-NMR (DMSO-d_6) (300 MHz): δ 0.86 (t, J = 7.2 Hz, 3H, piperidinyl NCH$_2$*CH*$_3$), 1.87 (d, J = 12.5 Hz, 1H, upfield H of piperidinyl *H*$_2$*C*-2"), 1.97 (s, 3H, pyrrolidinyl N*CH*$_3$), 2.14-2.23 (m, 1H, upfield H of piperidinyl N*CH*$_2$CH$_3$), 2.31-2.40 (m, 1H, downfield H of piperidinyl N*CH*$_2$CH$_3$), 2.85 (d, J = 14.9 Hz, 1H, upfield H of piperidinyl *H*$_2$*C*-6"), 3.23 (d, J = 12.7 Hz, 1H, downfield H of piperidinyl *H*$_2$*C*-2"), 3.28-3.41 (m, 2H, downfield H of

Paper View Article Online DOI: 10.1039/C4RA16663A RSC Advances

piperidinyl H_2C-6" + upfield H of pyrrolidinyl H_2C-5'), 3.74 (t, J = 9.7 Hz, 1H, downfield H of pyrrolidinyl H_2C-5'), 4.85 (dd, J = 10.4, 7.4 Hz, 1H, pyrrolidinyl *HC*-4'), 6.63 (d, J = 8.3 Hz, 1H, arom. H), 6.74 (d, J = 2.0 Hz, 1H, arom. H), 6.96-7.61 (m, 7H, arom. H + olefinic *CH*), 7.85 (d, J = 5.0 Hz, 1H, arom. H), 10.55 (s, 1H, NH). ^{13}C-NMR (DMSO-d_6) (75 MHz): δ 11.0 (piperidinyl NCH_2CH_3), 33.9 (pyrrolidinyl NCH_3), 34.7 (pyrrolidinyl H*C*-4'), 51.3 (piperidinyl NCH_2CH_3), 53.1 (piperidinyl H_2C-6"), 54.8 (piperidinyl H_2C-2"), 57.7 (pyrrolidinyl H_2C-5'), 64.0 [spiro *C*-3' (*C*-3")], 75.3 [spiro *C*-3 (*C*-2')], 109.9, 124.5, 124.7, 126.1, 126.6, 126.9, 128.4, 128.7, 128.9, 129.6, 132.3, 134.0, 137.5, 140.7, 142.5 (arom. *C* + olefinic *C*), 175.9 [indolyl *C*=O (*C*-2)], 196.6 [piperidinyl *C*=O (*C*-4")]. HRMS (ESI): *m/z* [M + H]$^+$ calcd for $C_{27}H_{26}ClN_3O_2S_2$: 524.1228,found: 524.1250.

1',1''-dimethyl-4'-(3-pyridinyl)-5''-[(3-pyridinyl)methylidene]-dispiro[3*H*-indole-3,2'-pyrrolidine-3',3''-piperidine]-2(1*H*),4''-dione (17). Obtained from reaction of **6**, **8** and **10**. Reaction time 12 h, colorless microcrystals from toluene, mp 209-211 °C, yield 0.75 g (81%). IR: ν_{max}/cm^{-1} 3150 (NH), 1705, 1686 (C=O), 1618, 1603. ^{1}H-NMR ($CDCl_3$) (300 MHz): δ 1.71 (d, J = 12.6 Hz, 1H, upfield H of piperidinyl H_2C-2"), 2.04 (s, 3H, piperidinyl NCH_3), 2.17 (s, 3H, pyrrolidinyl NCH_3), 2.96 (dd, J = 14.7, 2.4 Hz, 1H, upfield H of piperidinyl H_2C-6"), 3.23-3.38 (m, 3H, downfield H of piperidinyl H_2C-2" + downfield H of piperidinyl H_2C-6" + upfield H of pyrrolidinyl H_2C-5'), 3.92 (dd, J = 10.8, 8.7 Hz, 1H, downfield H of pyrrolidinyl H_2C-5'), 4.79 (dd, J = 10.8, 6.9 Hz, 1H, pyrrolidinyl *HC*-4'), 6.65 (d, J = 7.8 Hz, 1H, arom. H), 6.95-8.51 (m, 12H, 10 arom. H + olefinic *CH* + NH), 8.59 (d, J = 1.8 Hz, 1H, arom. H). ^{13}C-NMR (DMSO-d_6) (100 MHz): δ 34.5 (pyrrolidinyl NCH_3), 43.2 (piperidinyl NCH_3), 44.8 (pyrrolidinyl H*C*-4'), 56.3 (piperidinyl H_2C-6"), 56.8 (pyrrolidinyl H_2C-5'), 57.6 (piperidinyl H_2C-2"), 65.2 [spiro *C*-3' (*C*-3")], 75.4 [spiro *C*-3 (*C*-2')], 109.4, 121.4, 124.01, 124.04, 126.9, 127.4, 129.2, 130.8, 133.4, 134.6, 135.7, 137.1, 137.2, 143.6, 148.4, 149.7, 150.5, 150.8 (arom. *C* + olefinic *C*), 177.1 [indolyl *C*=O (*C*-2)], 198.3 [piperidinyl *C*=O (*C*-4")]. Anal. Calcd. for $C_{28}H_{27}N_5O_2$ (465.56): C, 72.24; H, 5.85; N, 15.04. Found: C, 72.49; H, 5.82; N, 15.19.

1''-Ethyl-1'-methyl-4'-(3-pyridinyl)-5''-[(3-pyridinyl)methylidene]-dispiro[3*H*-indole-3,2'-pyrrolidine-3',3''-piperidine]-2(1*H*),4''-dione (18). Obtained from reaction of **7**, **8** and **10**. Reaction time 12 h, pale yellow microcrystals from toluene, mp 204-206 °C, yield 0.84 g (88%). IR: ν_{max}/cm^{-1} 3142 (NH), 1701, 1686 (C=O), 1618, 1597. ^{1}H-NMR (DMSO-d_6) (300 MHz): δ 0.73 (t, J = 7.2 Hz, 3H, piperidinyl NCH_2CH_3), 1.73 (d, J = 12.0 Hz, 1H, upfield H of piperidinyl H_2C-2"), 1.98 (s, 3H, pyrrolidinyl NCH_3), 2.03-2.13 (m, 1H, upfield H of piperidinyl NCH_2CH_3), 2.17-2.25 (m, 1H, downfield H of piperidinyl NCH_2CH_3), 3.00-3.32 (m, 4H, upfield H of piperidinyl H_2C-6" + downfield H of piperidinyl H_2C-2" + downfield H of piperidinyl H_2C-6" + upfield H of pyrrolidinyl H_2C-5'), 3.78 (t, J = 9.8 Hz, 1H, downfield H of pyrrolidinyl H_2C-5'), 4.62 (dd, J = 9.9, 7.5 Hz, 1H, pyrrolidinyl *HC*-4'), 6.61 (d, J = 7.8 Hz, 1H, arom. H), 6.88-8.48 (m, 12H, 11 arom. H + olefinic *CH*), 10.41 (s, 1H, NH). ^{13}C-NMR (DMSO-d_6) (100 MHz): δ 11.2 (piperidinyl NCH_2CH_3), 34.4 (pyrrolidinyl NCH_3), 43.4 (pyrrolidinyl H*C*-4'), 51.5 (piperidinyl NCH_2CH_3), 53.5 (piperidinyl H_2C-6"), 56.6 (piperidinyl H_2C-2"), 56.8 (pyrrolidinyl H_2C-5'), 64.6 [spiro *C*-3' (*C*-3")], 75.9 [spiro *C*-3 (*C*-2')], 109.3, 121.4, 124.0, 124.1, 126.8, 127.4, 129.3, 130.9, 133.6, 134.7, 135.6, 137.1, 137.4, 143.8, 148.4, 149.7, 150.7, 150.9 (arom. *C* + olefinic *C*), 177.0 [indolyl *C*=O (*C*-2)], 198.7 [piperidinyl *C*=O (*C*-4")]. Anal. Calcd. for $C_{29}H_{29}N_5O_2$ (479.59): C, 72.63; H, 6.10; N, 14.60. Found: C, 72.86; H, 6.17; N, 14.78.

5-Chloro-1''-ethyl-1'-methyl-4'-(3-pyridinyl)-5''-[(3-pyridinyl)methylidene]-dispiro[3*H*-indole-3,2'-pyrrolidine-3',3''-piperidine]-2(1*H*),4''-dione (19). Obtained from reaction of **7**, **9** and **10**. Reaction time 11 h, colorless microcrystals from ethanol, mp 244-246 °C, yield 0.76 g (74%). IR: ν_{max}/cm^{-1} 3408 (NH), 1709, 1686 (C=O), 1616, 1593. ^{1}H-NMR (DMSO-d_6) (300 MHz): δ 0.74 (t, J = 7.1 Hz, 3H, piperidinyl NCH_2CH_3), 1.72 (d, J = 12.3 Hz, 1H, upfield H of piperidinyl H_2C-2"), 2.01 (s, 3H, pyrrolidinyl NCH_3), 2.09-2.26 (m, 2H, upfield H of piperidinyl NCH_2CH_3 + downfield H of piperidinyl NCH_2CH_3), 3.05-3.34 (m, 4H, upfield H of piperidinyl H_2C-6" + downfield H of piperidinyl H_2C-2" + downfield H of piperidinyl H_2C-6" + upfield H of pyrrolidinyl H_2C-5'), 3.77 (t, J = 9.6 Hz, 1H, downfield H of pyrrolidinyl H_2C-5'), 4.62 (dd, J = 9.9, 7.5 Hz, 1H, pyrrolidinyl *HC*-4'), 6.63 (d, J = 8.1 Hz, 1H, arom. H), 6.80-8.51 (m, 11H, 10 arom. H + olefinic *CH*), 10.59 (s, 1H, NH). ^{13}C-NMR (DMSO-d_6) (100 MHz): δ 11.2 (piperidinyl NCH_2CH_3), 34.5 (pyrrolidinyl NCH_3), 43.2 (pyrrolidinyl H*C*-4'), 51.5 (piperidinyl NCH_2CH_3), 53.5 (piperidinyl H_2C-6"), 56.6 (piperidinyl H_2C-2"), 56.9 (pyrrolidinyl H_2C-5'), 64.9 [spiro *C*-3' (*C*-3")], 75.9 [spiro *C*-3 (*C*-2')], 110.8, 124.0, 124.2, 125.5, 127.2, 129.0, 129.1, 130.7, 133.9, 134.4, 135.6, 137.2, 137.4, 142.7, 148.6, 150.0, 150.7, 150.9 (arom. *C* + olefinic *C*), 176.7 [indolyl *C*=O (*C*-2)], 198.4 [piperidinyl *C*=O (*C*-4")]. Anal. Calcd. for $C_{29}H_{28}ClN_5O_2$ (514.03): C, 67.76; H, 5.49; N, 13.62. Found: C, 67.91; H, 5.56; N, 13.81.

Single crystal X-ray

The X-ray single crystal diffraction data were collected at 120 K on an Agilent SuperNova instrument with focussed microsource Cu Kα radiation (λ = 1.5418 Å) and ATLAS CCD area detector. Details of the data collection conditions and the parameters of the refinement are given in Table 8.

RSC Advances View Article Online DOI: 10.1039/C4RA16663A Paper

Table 8 Crystal data and structure refinement parameters for compounds **3** and **14**.

Compound	**3**	**14**
Chemical formula	$C_{21}H_{17}Cl_4NO$	$C_{31}H_{28}ClF_2N_3O_2$
M_r	441.16	548.01
Crystal system, space group	Monoclinic, *C*2/*c*	Monoclinic, $P2_1/n$
Temperature (K)	120	120
a, *b*, *c* (Å)	21.5694(4), 7.0397(1), 25.8262(3)	11.97300 (13), 16.1952 (3), 14.09653 (16)
β (°)	90.325(1)	93.4721 (10)
V (Å^3)	3921.44(10)	2728.37 (6)
Z	8	4
Radiation type	Cu $K\alpha$	Cu $K\alpha$
μ (mm$^{-1)}$	5.577	1.64
Crystal size (mm)	0.22 x 0.18 x 0,14	0.30 × 0.24 × 0.06
Diffractometer	SuperNova (Cu) X-ray	SuperNova (Cu) X-ray
T_{min}, T_{max}	0.373, 0.509	0.721, 0.922
No. of measured, independent and observed [$I > 2\sigma(I)$] reflections	21368, 3540, 3137	38016, 4913, 4248
R_{int}	0.038	0.048
$(\sin\theta/\lambda)_{max}$ (Å^{-1})	0.599	0.599
$R[F^2 > 2\sigma(F^2)]$, $wR(F^2)$, S	0.027, 0.075, 1.01	0.036, 0.096, 1.05
No. of reflections	3540	4913
No. of parameters	244	356
$\Delta\rho_{max}$, $\Delta\rho_{min}$ (e Å^{-3})	0.29, -0.22	0.42, -0.23

The structures were solved using direct methods with SHELXS[60] and refined on F^2 using all data by full–matrix least square procedures with SHELXL–97.[60] Multiscan absorption corrections were done using SCALE3 ABSPACK. The non–hydrogen atoms were refined with anisotropic displacement parameters. All hydrogen atoms were included in calculated positions with isotropic displacement parameters 1.2 times the isotropic equivalent of their carrier atoms. Full crystallographic details of compounds **3** and **14** have been deposited at the Cambridge Crystallographic Data Centre (CCDC) as supplementary publication numbers CCDC 1037561 and CCDC 1028899, respectively.

Antitumor activity screening

Antitumor properties of the synthesized compounds **11-19** were screened by the National Cancer Institute, Cairo University, Egypt, using the reported *in-vitro* Sulfo-Rhodamine-B (SRB) standard technique adopting HeLa (cervical) and HepG2 (liver) human tumor cell lines.[43–49] Cells were seeded in 96-well microtiter plates at a concentration of 5 x 10^4 – 10^5 cell/well in a fresh medium and left for 24 h before treatment with the test compounds to allow attachment of cells to the wall of the plate. The test compounds were dissolved in dimethylsulfoxide (DMSO) and diluted 1000-fold in the assay. Different concentrations of the compounds under test (0, 2.5, 6.25, 12.5, and 25 μg/ml) were added to the cell monolayer. Triplicate wells were prepared for each individual dose. The monolayer cells were incubated with the test compounds for 48 h at 37 °C, in an atmosphere of 5% CO_2. After 48 h, the cells were fixed, washed and stained with Sulfo-Rhodamine-B (SRB) stain. Excess stain was washed with acetic acid. The attached stain was recovered with Tris-EDTA buffer. Cell survival and drug activity were determined by measuring the color intensity spectrophotometrically at 564 nm using an ELISA microplate reader (Meter tech. Σ 960, USA). Data are collected as mean values for experiments that were performed in three replicates for each individual dose which were measured by SRB assay. Control experiments did not exhibit significant change compared to the DMSO vehicle. Doxorubicin hydrochloride and cisplatin were used as standard references during the present *in-vitro* bioactivity screening assay. The percentage of cell survival was calculated according to equation (4).

$$Surviving\ fraction = \frac{Optical\ density\ (O.D.)of\ treated\ cells}{O.D.of\ contol\ cells} \quad \ldots\ldots(4)$$

The IC_{50} (concentration required to produce 50% inhibition of cell growth compared to control experiment) was determined using Graph-Pad PRISM version-5 software. Statistical calculations for determination of the mean and standard error values were determined using SPSS 16 software. The observed antitumor properties are presented in Table 1 (Figures S33, and S34 of supplementary material).

Acknowledgements

This study was supported financially by the Science and Technology Development Fund (STDF), Egypt, Grant No. 1357.

Notes and references

[a]*Pesticide Chemistry Department, National Research Centre, Dokki, Cairo 12622, Egypt*
[b]*Center for Heterocyclic Compounds, Department of Chemistry, University of Florida, Gainesville, FL 32611-7200, USA. E-mail: charlesdennishall@gmail.com, tel: +1-352-392-0554*
[c]*Chemistry Department, University of Canterbury, Christchurch, New Zealand.*
[d]*Department of Chemistry, King Abdulaziz University, Jeddah, 21589, Saudi Arabia*

Electronic Supplementary Information (ESI) available: Copy of IR, 1H NMR, 13C NMR, HRMS/elemental analysis, HSQC and pharmacological graphs of synthesized the compounds. See DOI: 10.1039/b000000x/

1. H. Frankish, *Lancet*, 2003, **361**, 1278.
2. D. Belpomme, P. Irigaray, A. J. Sasco, J. A. Newby, V. Howard, R. Clapp, L. Hardell, *Int. J. Oncol.*, 2007, **30**, 1037–1049.
3. C. Are, S. Rajaram, M. Are, H. Raj, B. O. Anderson, R. C. Swamy, M. Vijayakumar, T. Song, M. Pandey, J. A. Edney, E. L. Cazap, *J. Surg. Oncol.*, 2013, **107**, 221–226.
4. E. Carrasco, P. J. Álvarez, C. Melguizo, J. Prados, E. Álvarez-Manzaneda R. Chahboun, I. Messouri, M. I. Vázquez-

View Article Online
DOI: 10.1039/C4RA16663A RSC Advances

Vázquez, A. Aránega, F. Rodríguez-Serrano, *Eur. J. Med. Chem.*, 2014, **79**, 1–12.
5. C. W. Mai, M. Yaeghoobi, N. Abd-Rahman, Y. B. Kang, M. R. Pichika, *Eur. J. Med. Chem.*, 2014, **77**, 378–387.
6. K. Singh, V. Verma, K. Yadav, V. Sreekanth, D. Kumar, A. Bajaj, V. Kumar, *Eur. J. Med. Chem.*, 2014, **87**, 150−158.
7. A. S. Girgis, S. S. Panda, E. S. M. Shalaby, A. F. Mabied, P. J. Steel, C. D. Hall, A. R. Katritzky, *RSC Adv*., 2015, **5**, 14780−14787.
8. S. Nishio, K. Ushijima, T. Yamaguchi, Y. Sasajima, H. Tsuda, T. Kasamatsu, M. Kage, M. Ono, M. Kuwano, T. Kamura, *Gynecol. Oncol.*, 2014, **132**, 703–708.
9. A. Jemal, F. Bray, M. M. Center, J. Ferlay, E. Ward, D. Forman, *CA Cancer J. Clin.*, 2011, **61**, 69–90.
10. M. Abbas, K. Srivastava, M. Imran, M. Banerjee, *Eur. J. Obstet. Gynecol. Reprod. Biol.*, 2014, **176**, 68–74.
11. R. Siegel, D. Naishadham, A. Jemal, *CA Cancer J. Clin.*, 2012, **62**, 10–29.
12. J. M. Walboomers, M. V. Jacobs, M. M. Manos, F. X. Bosch, J. A. Kummer, K. V. Shah, P. J. Snijders, J. Peto, C. J. Meijer, N. Muñoz, *J. Pathol.*, 1999, **189**, 12–19.
13. R. D. Burk, A. Harari, Z. Chen, *Virology*, 2013, **445**, 232–243.
14. V. Cogliano, R. Baan, K. Straif, Y. Grosse, B. Secretan, F. El Ghissassi, *Lancet Oncol.*, 2005, **6**, 204.
15. J. S. Smith, L. Lindsay, B. Hoots, J. Keys, S. Franceschi, R. Winer, G. M. Clifford, *Int. J. Cancer*, 2007, **121**, 621–632.
16. E. M. Burd, *Clin. Microbiol. Rev.*, 2003, **16**, 1–17.
17. S. Muthusami, D. S. Prabakaran, J.-R. Yu, W.-Y. Park, *Cancer Lett.*, 2014, **351**, 252–259.
18. C. P. Harris, X. L. Lu, G. Narayan, B. Singh, V. V. V. S. Murty, Genes Chromosomes Cancer 36 (2003) 233–241.
19. L. Scotto, G. Narayan, S. V. Nadula, H. Arias-Pulido, S. Subramaniyam, A. Schneider, A. M. Kaufmann, J. D. Wright, B. Pothuri, M. Mansukhani, V. V. Murty, *Genes Chromosomes Cancer*, 2008, **47**, 755–765.
20. D. Lorusso, F. Petrelli, A. Coinu, F. Raspagliesi, S. Barni, *Gynecol. Oncol.*, 2014, **133**, 117–123.
21. F. Landoni, E. Sartori, T. Maggino, P. Zola, V. Zanagnolo, S. Cosio, F. Ferrari, E. Piovano, A. Gadducci, *Gynecol. Oncol.*, 2014, **132**, 611–617.
22. C. Vale, J. F. Tierney, L. Stewart, M. Brady, K. Dinshaw, A. Jakobsen, M. K. B. Parmar, G. Thomas, T. Trimble, D. S. Alberts, H. Chen, S. Cikaric, P. J. Eifel, M. Garipagaoglu, H. Keys, N. Kantardzic, P. Lal, R. Lanciano, F. Leborgne, V. Lorvidhaya, H. Onishi, R. G. Pearcey, E. Pras, K. Roberts, P. G. Rose, C. W. Whitney, *J. Clin. Oncol.*, 2008, **26**, 5802–5812.
23. L. A. Rojas-Espaillat, P. G. Rose, *Curr. Opin. Oncol.*, 2005, **17**, 485–492.
24. A. Dueñas-González, J. J. Zarbá, F. Patel, J. C. Alcedo, S. Beslija, L. Casanova, P. Pattaranutaporn, S. Hameed, J. M. Blair, H. Barraclough, M. Orlando, *J. Clin. Oncol.*, 2011, **29**, 1678–1685.
25. A. Abe, H. Furumoto, M. Nishimura, M. Irahara, H. Ikushima, *Oncol. Lett.*, 2012, **3**, 571–576.
26. R. Das, K. Bhattacharya, S. K. Samanta, B. C. Pal, C. Mandal, *Cancer Lett.*, 2014, **351**, 81–90.
27. S. Schott, A. Brüning, *Gynecol. Oncol.*, (in press)
28. J. F. De Los Santos, Jr. J. M. Straughn, http://www.uptodate.com/contents/management-of-locally-advancedcervical-cancer
29. J. H. Maduro, E. Pras, P. H. Willemse, E. G. de Vries, *Cancer Treat. Rev.*, 2003, **29**, 471–488.
30. Z. H. Siddik, *Oncogene*, 2003, **22**, 7265–7279.
31. X. Li, L. Ran, W. Fang, D. Wang, *Biomedicine Pharmacotherapy*, 2014, **68**, 291–297.
32. A. Jemal, R. Siegel, E. Ward, Y. Hao, J. Xu, M. J. Thun, Cancer statistics, *CA Cancer J. Clin.*, 2009, **59**, 225–249.
33. Y. Bai, Y. Xue, X. Xie, T. Yu, Y. Zhu, Q. Ge, Z. Lu, *Gene*, 2014, **548**, 91–100.
34. D. M. Parkin, *Int. J. Cancer*, 2006, **118**, 3030−3044.
35. H. B. El-Serag, *Gastroenterology*, 2012, **142**, 1264−1273.
36. J. Yu, J. Z. Yang, S. W. Su, *HeraldMed.*, 2013, **32**, 174−177.
37. T. Hirai, Y. Korogi, K. Ono, K. Maruoka, K. Harada, S. Aridomi, M. Takahashi, *Cardiovasc. Intervent. Radiol.*, 2001, **24**, 176−179.
38. A. R. de Lope, S. Tremosini, A. Forner, M. Reig, J. Bruix, *J. Hepatol.*, 2012, **56**, S75−S87.
39. J. M. Llovet, S. Ricci, V. Mazzaferro, P. Hilgard, E. Gane, J. F. Blanc, A. C. de Oliveira, A. Santoro, J.-L. Raoul, A. Forner, M. Schwartz, C. Porta, S. Zeuzem, L. Bolondi, T. F. Greten, P. R. Galle, J.-F. Seitz, I. Borbath, D. Häussinger, T. Giannaris, M. Shan, M. Moscovici, D. Voliotis, J. Bruix, N. *Engl. J. Med.*, 2008, **359**, 378−390.
40. J. Wu, Y. Zhang, Y. Cai, J. Wang, B. Weng, Q. Tang, X. Chen, Z. Pan, G. Liang, S. Yang, *Bioorg. Med. Chem.*, 2013, **21**, 3058–3065.
41. A. S. Girgis, F. H. Osman, F. A. El-Samahy, I. S. Ahmed-Farag, *Chem. Pap.* 60 (2006) 237−242.
42. R. Grigg, S. Thianpatanagul, *J. Chem. Soc., Chem. Commun.* (1984) 180−181.
43. R. F. George, N. S. M. Ismail, J. Stawinski, A. S. Girgis, *Eur. J. Med. Chem.*, 2013, **68**, 339–351.
44. A. M. Moustafa, A. S. Girgis, S. M. Shalaby, E. R. T. Tiekink, *Acta Crystallogr., Sect. E: Struct. Rep. Online*, 2012, **E68**, o2197–o2198.
45. A. S. Girgis, J. Stawinski, N. S. M. Ismail, H. Farag, *Eur. J. Med. Chem.*, 2012, **47**, 312–322.
46. A. R. Katritzky, A. S. Girgis, S. Slavov, S. R. Tala, I. Stoyanova-Slavova, *Eur. J. Med. Chem.*, 2010, **45**, 5183–5199.
47. A. S. Girgis, *Eur. J. Med. Chem.*, 2009, **44**, 1257–1264.
48. A. S. Girgis, *Eur. J. Med. Chem.*, 2009, **44**, 91–100.
49. A. S. Girgis, H. M. Hosni, F. F. Barsoum, *Bioorg. Med. Chem.*, 2006, **14**, 4466–4476.
50. A. S. Girgis, H. Farag, N. S. M. Ismail, R. F. George, *Eur. J. Med. Chem.*, 2011, **46**, 4964−4969.
51. A. S. Girgis, N. S. M. Ismail, H. Farag, *Eur. J. Med. Chem.*, 2011, **46**, 2397−2407.
52. A. S. Girgis, N. S. M. Ismail, H. Farag, W. I. El-Eraky, D. O. Saleh, S. R. Tala, A. R. Katritzky, *Eur. J. Med. Chem.*, 2010, **45**, 4229−4238.
53. A. S. Girgis, S. S. Panda, I. S. Ahmed Farag, A. M. El-Shabiny, A. M. Moustafa, N. S. M. Ismail,G. G. Pillai,C. S. Panda, C. D. Hall, A. R. Katritzky, *Org. Biomol. Chem.*, 2015, 13, 1741−1753.
54. A. D. Tiwari, S. S. Panda, A. S. Girgis,S. Sahu, R. F. George, A. M. Srour, B. La Starza, A. M. Asiri, C. D. Hall, A. R. Katritzky, *Org. Biomol. Chem.*, 2014, **12**, 7238−7249.
55. I. S. Ahmed Farag, A. S. Girgis, A. M. Moustafa, B. E. M. El-Gendy, A. F. Mabied, E. M. Shalaby, *J. Mol. Struct.*, 2014, **1075**, 327−334.
56. CODESSA-Pro Manual, pages 54,55,58,63
57. Z. Liu, J. L. Medina-Franco, R. A. Houghten, M. A. Giulianotti, *Tetrahedron Lett.*, 2010, **51**, 5003–5004.

RSC Advances
View Article Online
DOI: 10.1039/C4RA16663A
Paper

58. F. A. M. Al-Omary, G. S. Hassan, S. M. El-Messery, H. I. El-Subbagh, *Eur. J. Med. Chem.*, 2012, **47**, 65−72.
59. S. Z. Vatsadze, M. A. Manaenkova, N. V. Sviridenkova, N. V. Zyk, D. P. Krut´ko, A. V. Churakov, M. Yu. Antipin, J. A. K. Howard, H. Lang, Russian *Chem. Bull., International Ed.*, 2006, **55**, 1184−1194.
60. G. M. Sheldrick, *Acta Crystallogr., Sect. A*, 2008, **64**, 112−122.

View Article Online
DOI: 10.1039/C4RA16663A

Graphical abstract

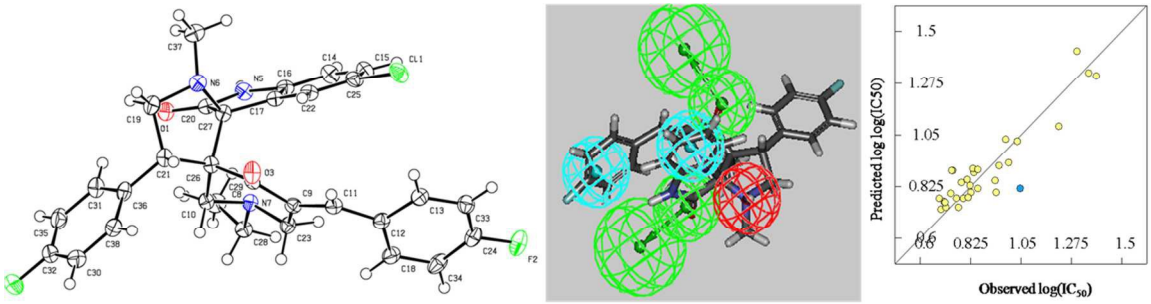

A series of novel substituted dispiro-oxindole were synthesized and screened for anti-cancer properties. The anti-cancer data were validated by QSAR studies.